Summer 7-19-2011

Synthesis and Characterization of Metal Nanoclusters Stabilized by Dithiolates

Donald A. Robinson III
Georgia State University, drobinson45@student.gsu.edu

SYNTHESIS AND CHARACTERIZATION OF

METAL NANOCLUSTERS STABILIZED BY DITHIOLATES

by

DONALD ARLINGTON ROBINSON, III

Under the Direction of Dr. Gangli Wang

ABSTRACT

Rapidly expanding research in nanotechnology has led to exciting progress in a versatile array of applications from medical diagnostics to photocatalytic fuel cells. Such success is due to the ability of researchers to manipulate the desired properties of nanomaterials by controlling their size, shape, and composition. Among the most thriving areas of nanoparticle research has been the synthesis and characterization of stable metallic nanoclusters capped by thiolate ligands. Our group has extended this research to study copper, silver, and gold clusters with remarkable stability and energetics, which was achieved by using dithiolates as the ligand stabilizers. In addition to the enhanced stability offered by the chelate effect, the use of dithiolate ligands instead of monothiolates is proposed to provide an alternate interfacial bond structure that is shown to strongly influence energetic properties of nanoclusters, with strong evidence of metal-ligand charge transfer. Energetic properties were characterized by spectroscopic and electrochemical methods.

INDEX WORDS: Nanocluster, Copper, Silver, Gold, Dithiolate, Voltammetry, Electrochemistry, Absorption, Fluorescence

SYNTHESIS AND CHARACTERIZATION OF METAL NANOCLUSTERS STABILIZED BY DITHIOLATES

by

DONALD ARLINGTON ROBINSON, III

A Thesis Submitted in Partial Fulfillment of the Requirements for the Degree of

Master of Science

in the College of Arts and Sciences

Georgia State University

2011

SYNTHESIS AND CHARACTERIZATION OF METAL NANOCLUSTERS STABILIZED BY DITHIOLATES

by

DONALD ARLINGTON ROBINSON, III

Committee Chair: Dr. Gangli Wang

Committee: Dr. Markus Germann
Dr. Gabor Patonay
Dr. Hao Xu

Electronic version approved:

Office of Graduate Studies

College of Arts and Sciences

Georgia State University

December 2011

DEDICATION

I dedicate this work to the memory of my father, Donald Arlington Robinson, Jr. I also devote this to my wonderful family; especially my mother, Mary, and my wife, Caroline, for their overwhelming love and cherished support.

ACKNOWLEDGEMENTS

I express the utmost gratitude to Dr. Gangli Wang for the opportunity to work on this fascinating project and for all the motivation and guidance he has provided. I want to also thank my colleague, Zhenghua Tang for training me in the laboratory and for all his collaborative efforts. Additionally, I thank Dr. Dabney Dixon for all her tips on good presentation and professionalism. I am also very appreciative for the assistance from Hui Zhao of the GSU AFM laboratory and Dr. Siming Wang along with all the members of the GSU mass spectrometry facility. And last but not least, I would like to recognize the collective teamwork from all the members of the Gangli Wang research group, who have greatly inspired me throughout my time here at Georgia State University.

TABLE OF CONTENTS

LIST OF TABLES

LIST OF FIGURES

LIST OF ABBREVIATIONS

A	surface area of electrode
AFM	atomic force microscopy
C	concentration
CS	captopril
CV	cyclic voltammetry/voltammogram
D	diffusion coefficient
DCM	dichloromethane
DMSA	dimercaptosuccinic acid
DOSY	diffusion-ordered spectroscopy
DPV	differential pulse voltammetry/voltammogram
DTC	dithiolate-protected cluster
Durene-DT	durene-(α1, α2)-dithiol
E	energy
E_{chg}	charging energy
E_{gap}	electrochemical band gap energy
E_{opt}	optical band gap energy
ECHEM	electrochemistry
ESI	electrospray ionization
ET	electron transfer
FTIR	Fourier-transform infrared
4-FTP	4-fluorothiophenol
GS	glutathione
H_2MSA	mercaptosuccinic acid
HOMO	highest occupied molecular orbital
i_p	peak current
IR	infrared
LA	alpha(+/-) lipoic acid
LUMO	lowest unoccupied molecular orbital
MALDI	matrix-assisted laser desorption ionization
MPC	monothiolate-protected cluster
MS	mass spectrometry
MTC	mixed-thiolate protected cluster
n	number of atoms, number of electrons transferred
n_{Dur}	number of durene-DT electrons transferred
n_{QDL}	number of electrons transferred in gold core by QDL charging
NIR	near-infrared
NMR	nuclear magnetic resonance
ORR	oxygen reduction reaction
PAGE	polyacrylamide gel electrophoresis
PhC_2S	phenylethanethiol
PL	photoluminescence
QDL	quantized double layer charging
R_4N^+	quarternary ammonium cation

RT	room temperature
SH	thiol
SPR	surface plasmon resonance
SR	generic monothiolate ligand
TBAP	tetrabutylammonium perchlorate
TEM	transmission electron microscopy
TOA	tetraoctylammonium
UV	ultraviolet
v	scan rate
$_{\Delta}V$	change in potential, charging energy
Vis	visible
X	halide
XPS	x-ray photoelectron spectroscopy

1. INTRODUCTION

1.1 Metal Nanoparticles and Thiolate-Stabilized Metal Nanoclusters

Great advances have been achieved in recent decades toward the development of metallic nanoparticles with control over size, shape, and composition in order to fine tune the desired properties.[1] Tailoring the properties of nanoparticles is important for various applications, including medicine,[2-4] nanoelectronics,[2,5,6] and catalysis.[2,5,7] Many different types of ligands and ionic surfactants[8-12] can be used to stabilize nanoparticles and control their growth. The most popular ligand stabilizers include ligands such as carboxylates,[13,14] amines,[15-17] thiolates,[8-12] and dendrimers.[18-20] Our group focuses on thiolates as stabilizers, as they have so far proven to be the most suitable ligands in a solution-based synthesis to effectively control the aggregation of noble metal atoms and ultimately form stable nanoclusters* with high monodispersity (i.e. uniform size, shape, and composition).[8-12] We propose that dithiolates will provide even stronger enhancement to stability due to entropy gain.[21] Shown in Figure 1 is a simplified model for the monothiolate-protected cluster (MPC), composed of one spherical cluster of zerovalent metal atoms forming the core with the ligands (in this case monothiolates), forming a protective monolayer shell around the cluster.

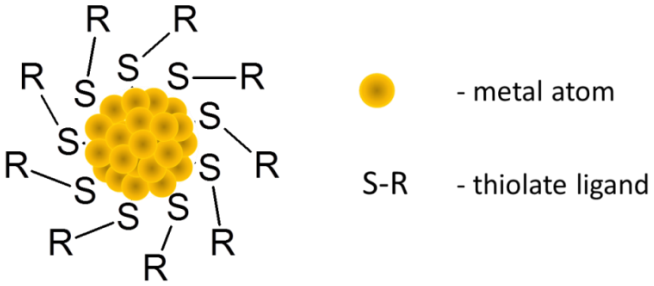

Figure 1. Cartoon illustrating the basic structure of a metal nanocluster protected by monothiolate ligands.

* Although the terms "nanoparticle" and "nanocluster" are commonly used interchangeably, for the purpose of this report, "nanocluster" will be used to distinguish a more specific family of metal nanoparticles, spherical or ellipsoidal in shape, and less than 10 nm in diameter.

MPCs of various transition metal cores have been synthesized, including but not limited to platinum, palladium, gold, silver, and copper. Gold is by far the most well-researched core metal for MPC synthesis and characterization, as shown in the pie chart in Figure 2. Gold's popularity in nanoparticle and self-assembled monolayer research is largely based on its relative inertness (e.g. resistance to oxidation), yet strong binding affinity for thiolates.[22,23] Therefore gold has many of the same advantages of platinum and palladium without the cost. Of course, gold is still very expensive, and it would be ideal to expand the research base to more cost effective transition metals. Silver ranks in a distant 2nd place for overall depth of research. Elemental silver, however, can react with atmospheric oxygen under ambient conditions, so a more careful synthesis is required. The most difficult metal to work with out of the five listed below is copper, which is the most reactive, thus making the synthesis of stable copper nanoclusters a very challenging task. However, the affinity of copper and silver to thiolates is comparable to that of gold, so thiolates are preferred over other ligands such as amines or carboxylates.[24]

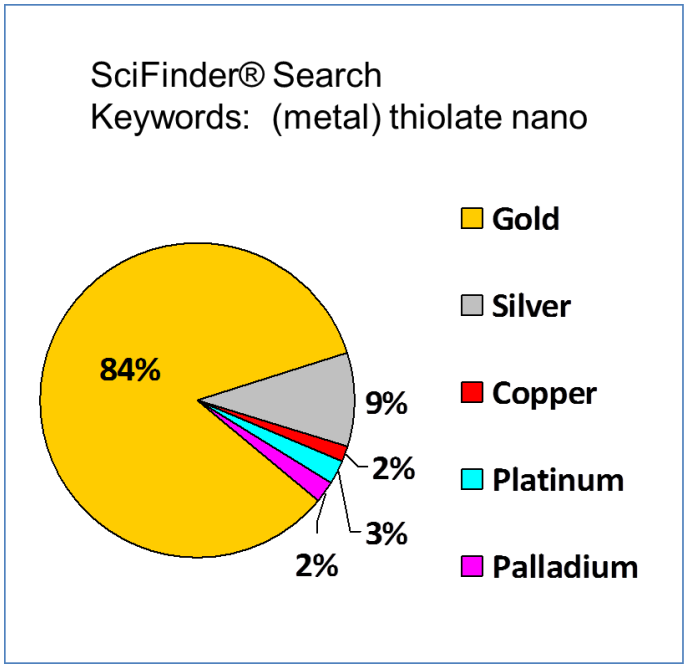

Figure 2. Results of a SciFinder® search for various thiolate-protected metal nanoparticles.

1.2 Gold Nanoclusters

While gold nanoparticles have been synthesized using non-thiolate ligands such as amines,[25] carboxylates,[14] and dendrimers,[26] the particles synthesized by these methods are primarily large in size and relatively polydispersed. Gold nanoclusters synthesized using thiolate ligands are generally smaller and more monodispersed in comparison. Due to the extensive literature background on gold monothiolate-protected clusters (AuMPCs), a concise review of AuMPC research serves as an appropriate introduction to metal nanoclusters in general. It should be noted that the characteristics of metal nanoclusters composed of different metal cores (e.g. copper, silver, platinum) are not expected to mimic the properties of AuMPCs based on similarities in size, shape, or metal atom core composition. However, the experimental methods used to investigate AuMPCs have proven relevant and necessary in the characterization of nanocluster species with alternative metal and/or ligand types, as evidenced in the chapters to come.

1.2.1 Synthesis of AuMPCs

A general outline of the synthesis of AuMPCs is shown in Figure 3. The most commonly used synthetic procedure is the Brust-Schriffin method,[27] which involves a two-phase aqueous and organic system. First, an aqueous solution of the gold salt is mixed with a solution of the quaternary ammonium phase-transfer reagent (R_4N^+) in nonpolar organic solvent (commonly toluene). The aqueous phase is usually removed after all of the gold is transferred to the organic phase. Next, the desired thiol compound is added to the organic phase, resulting in a color change from dark yellow/orange to colorless solution, indicating the reduction of Au^{3+} to Au^+. The final step involves the addition of excess sodium borohydride in aqueous solution. The borohydride reduces Au^+ to Au^0, resulting in nanoparticle nucleation and growth, which is controlled, contained, and evolved by thiolate ligation, ultimately resulting in AuMPCs. A

mixed-solvent one phase method can also be used, whereby the gold salt and thiols are reacted together in a polar organic solvent, such as THF. The second step is similar to the two-phase method, whereby excess sodium borohydride in water is added to achieve complete reduction of gold and trigger AuMPC formation.[9,28] Water-soluble AuMPCs have also been prepared without the use of phase-transfer reagents in water/methanol mixed solvent reaction systems[29,30] and all-aqueous systems[31,32] using thiols with polar functionalities.

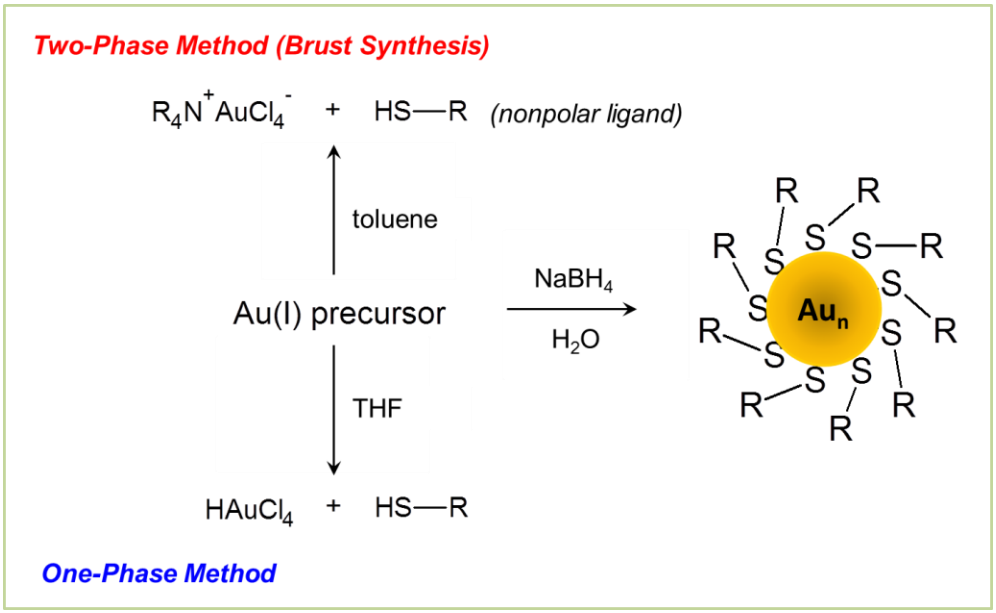

Figure 3. Diagram for the synthesis of AuMPCs, one-phase and two-phase approaches.

The mechanistic details of AuMPC synthesis are poorly understood, although researchers have made significant progress in recent years.[33-36] The Au(I) precursor of the two-phase method was generally assumed to be a polymeric Au(I)-thiolate complex. Such polymers could be observed by dynamic light scattering and the size uniformity of these polymers was confirmed to affect the monodispersity of resulting AuMPCs.[10] Yet, under anhydrous conditions the precursor was determined by Goulet and Lennox to be a complex of Au(I) with R_4N^+.[33] The thiols, upon reduction of Au(III), are in turn oxidized to disulfides. However, for one-phase methods in which

polar solvents are employed, Au(I) thiolate complexes are in fact the precursors. It was later discovered that the R_4N^+ actually forms an inverse micelle structure with the anionic gold halide complex for both the Au(III) and Au(I) species.[34] It was further revealed that if water is present during thiol mixing, the resulting precursor is a mixture of a $[R_4N^+][AuX_2]$ complex micelles and polymeric $[Au(I)SR]_n$. The amount of water present after phase-transfer is important for the composition of this mixture. As more water is introduced, the amount of $[Au(I)SR]_n$ increases. Water is encapsulated inside the polar core of the inverse micelles and was found to function as a proton acceptor to remove the thiol proton, thus facilitating the formation of $[Au(I)SR]_n$ polymers.[35] This mechanistic detail also explains why $[Au(I)SR]_n$ polymers are the observed precursor in the one-phase syntheses using polar solvents. After the addition of sodium borohydride, the evolution of AuMPC size is controlled by the amount of thiol in the system. It has been shown repeatedly that smaller, more monodispersed AuMPCs are resulted from syntheses that use relatively higher thiol:Au synthetic ratios.[32,37,38]

1.2.2 Structure of the AuMPC

The thiolate-gold interfacial bonding structure on the nanocluster surface remained a mystery for the greater period of AuMPC research, until the elucidation of the "staple" motif in 2008.[39] More recently, complete structures have been experimentally resolved for a select few AuMPC compositions, including $Au_{25}(SR)_{18}$, $Au_{38}(SR)_{24}$, and $Au_{102}(SR)_{44}$ by X-ray crystallography.[40-43] The crystal structure of $Au_{25}(SR)_{18}$ is shown in Figure 4, along with different monothiolate ligands that have been used to successfully synthesize the AuMPC with monodispersity. The core structure consists of thirteen gold atoms total, as one gold atom is entrapped within a dodecahedral Au_{12} cage. The remaining 12 gold atoms participate in thiolate-Au bonding,

forming the staple-like S-Au-S-Au-S structure. Both gold core and interfacial bonding structures contribute to the energetic properties of AuMPCs, which is discussed next.

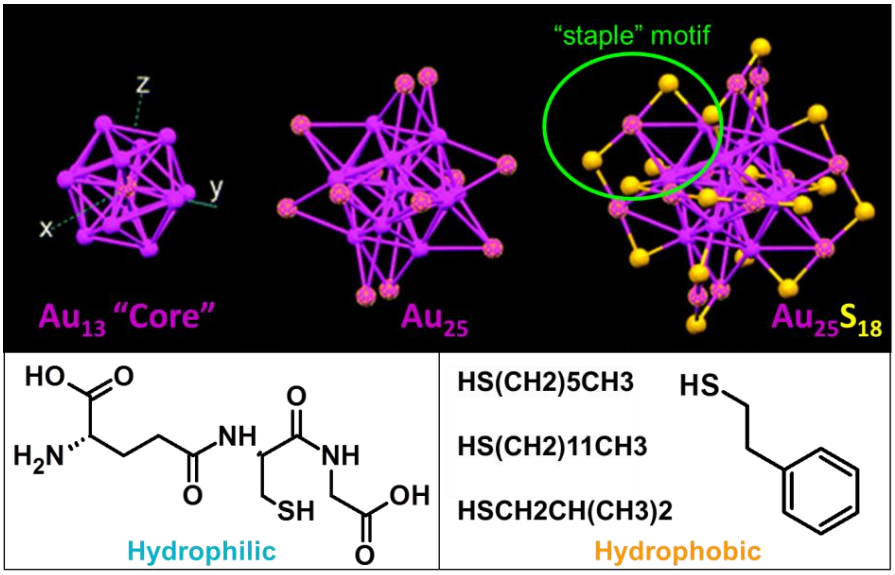

Figure 4. Crystal structure of $Au_{25}(SR)_{18}$ [image taken without permission from ref. 41]. Thiolate ligands (SR) that have proven effective in the synthesis of Au_{25}MPCs are shown in bottom panel.[10,44-46]

1.2.3 Energetics of the AuMPC

The energetic properties for AuMPCs have been extensively studied.[6,47,48] The characteristics of gold nanoparticles differ drastically from those of bulk gold, and these differences become more substantial with decreasing particle size, due to quantum confinement. For the especially small AuMPCs (75 gold atoms or less), optical and electrochemical features resemble those of a small complex. Slightly larger AuMPCs such as $Au_{144}(SR)_{60}$ exhibit energetics at the transition between small molecule and bulk gold. Fascinating energetics has been detected for AuMPCs, primarily using UV/Vis absorption spectroscopy, fluorescence spectroscopy, and electrochemical methods.

1.2.3.1 Optical Absorption

One optical property of gold that is widely exploited for biosensing is its surface plasmon resonance (SPR). For metal nanoparticles, localized surface plasmons occur, which are collective charge oscillations in the particle after excitation by light. This phenomenon can be detected by UV/Vis absorption spectroscopy as the so-called SPR band, which for spherical gold nanoparticles generally has a 520 nm wavelength. However, for AuMPCs smaller than 2 nm in diameter, the SPR absorption band is not visible. Discrete optical features appear for monodispersed AuMPCs, as shown in Figure 5.[38] The absorption spectrum for $Au_{144}(SR)_{60}$ consists of weak shoulders[49] while that of $Au_{25}(SR)_{18}$, which falls into the small molecule category, displays more discrete absorption peaks.[45,50]

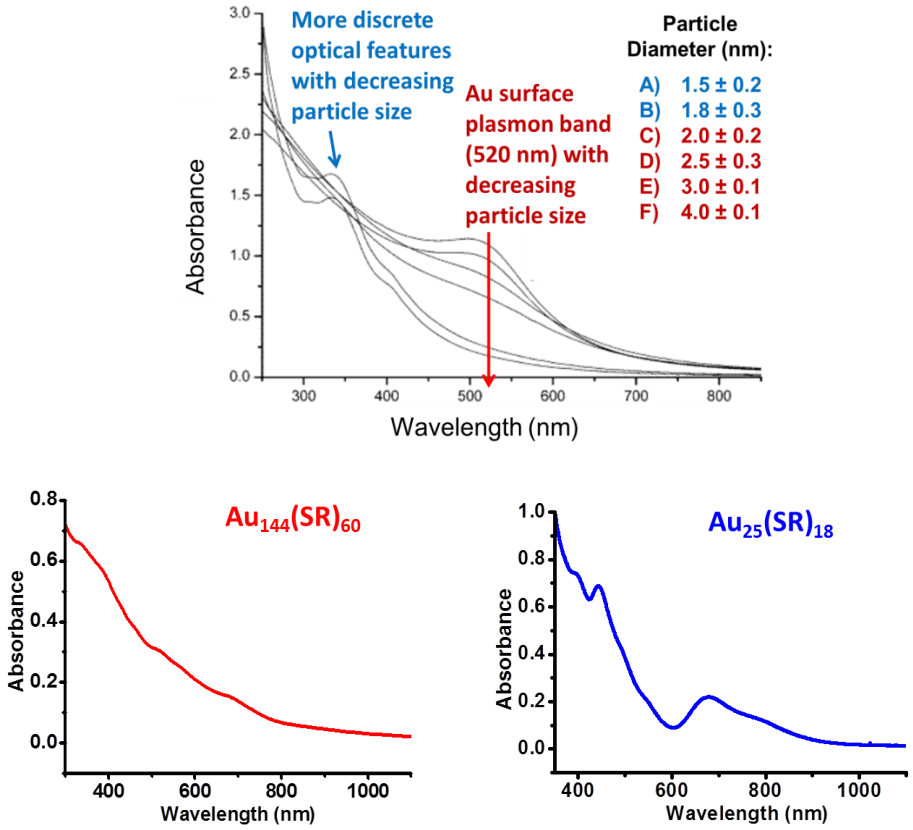

Figure 5. (a) UV/Vis absorption spectra for AuMPCs of varying core sizes. [image taken without permission from ref. 38] **(b)** Absorption spectrum for $Au_{144}(PhC_2S)_{60}$. **(c)** Absorption spectrum for $Au_{25}(PhC_2S)_{18}$.

1.2.3.2 Electrochemistry

The electrochemical properties of AuMPCs also clearly demonstrate the effects of quantum confinement. Differential pulse voltammograms (DPV) for both $Au_{144}(SR)_{60}$ and $Au_{25}(SR)_{18}$ are displayed below in Figure 6.[51,52] These AuMPCs are too small to exhibit the continuum charging behavior of bulk gold. A single nanocluster's double-layer capacitance (C) upon electron transfer is substantially increased as nanocluster size is decreased. In turn, the change in potential (ΔV) is increased for smaller nanocluster size (Equation 1).

$$\Delta V = ze/C \qquad (1)$$

Therefore, each electron transfer to and from the AuMPC can be specifically detected by voltammetry, termed "quantized double-layer charging."[6] For $Au_{144}(SR)_{60}$, several continuous quantized double-layer charging events are observed, each separated by a regular peak spacing, which is known as the charging energy, analogous to ΔV.

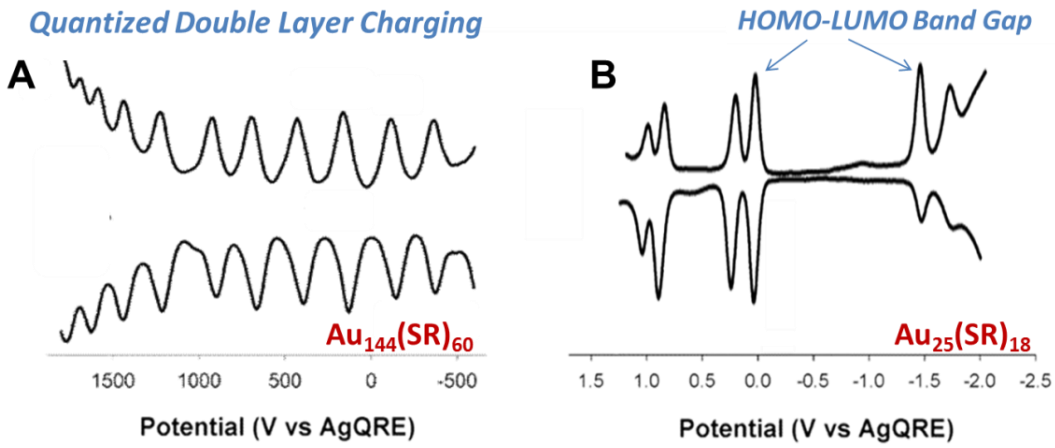

Figure 6. (a) Differential pulse voltammogram for $Au_{144}(SR)_{60}$ [image taken without permission from ref. 51] **(b)** Differential pulse voltammogram for $Au_{25}(SR)_{18}$. [image taken without permission from ref. 52]

In contrast to the continuous charging behavior of $Au_{144}(SR)_{60}$, the voltammetric response of $Au_{25}(SR)_{18}$ presents a large electrochemical band gap between the first oxidation current peak

and the first reduction peak. Equating the energetics of $Au_{25}(SR)_{18}$ to that of a small molecule, this electrochemical band gap is interpreted as an estimate for the energy difference between the HOMO and LUMO. The pair of peaks at ca. 0.2 V represents the two electron transfers to/from the HOMO while the pair of peaks at ca. -1.5 V is attributed to the LUMO. At ca. 1.0 V, yet another pair is resolved, indicating a molecular orbital at an even lower energy state. Each pair of peaks is separated by a relatively uniform charging energy. An energy diagram was constructed based on the correlation of electrochemical band gap values from voltammetry to the HOMO-LUMO optical band gap value determined from the onset of UV/Vis absorption, as shown in Figure 7.[52]

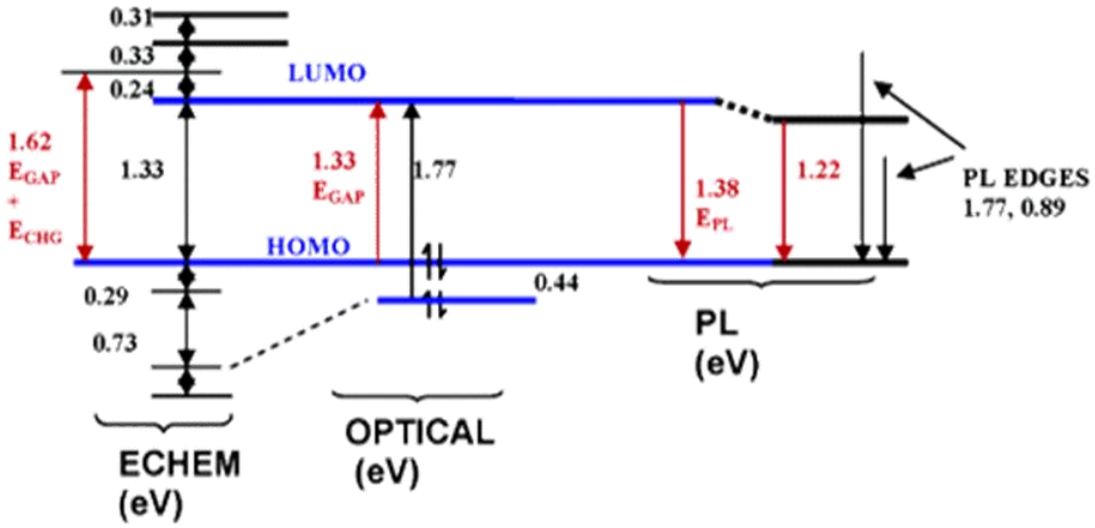

Figure 7. Energy diagram correlating optical and electrochemical responses, using a combination of optical band values from UV/Vis absorption spectroscopy and electrochemical band gap values from voltammetry [image taken without permission from ref. 52].

Using similar experimental techniques, the HOMO-LUMO band gaps were determined for many more AuMPC compositions. The diagram in Figure 8 displays the general trend for HOMO-LUMO band gaps with respect to Au core composition for the smaller AuMPCs (Au_{75}, Au_{55}, Au_{38}, Au_{25}, and Au_{13}). As gold core size decreases, the respective HOMO-LUMO band gap energy increases. The larger AuMPC species (Au_{225} and Au_{140}) do not exhibit HOMO-

LUMO small molecule energetics, but are compared based on the magnitude of relative quantized charging energies, which decreases as gold nanoparticle compositions grow larger until the voltammetric response is no longer quantized but instead represents the continuum charging behavior of bulk gold.[6]

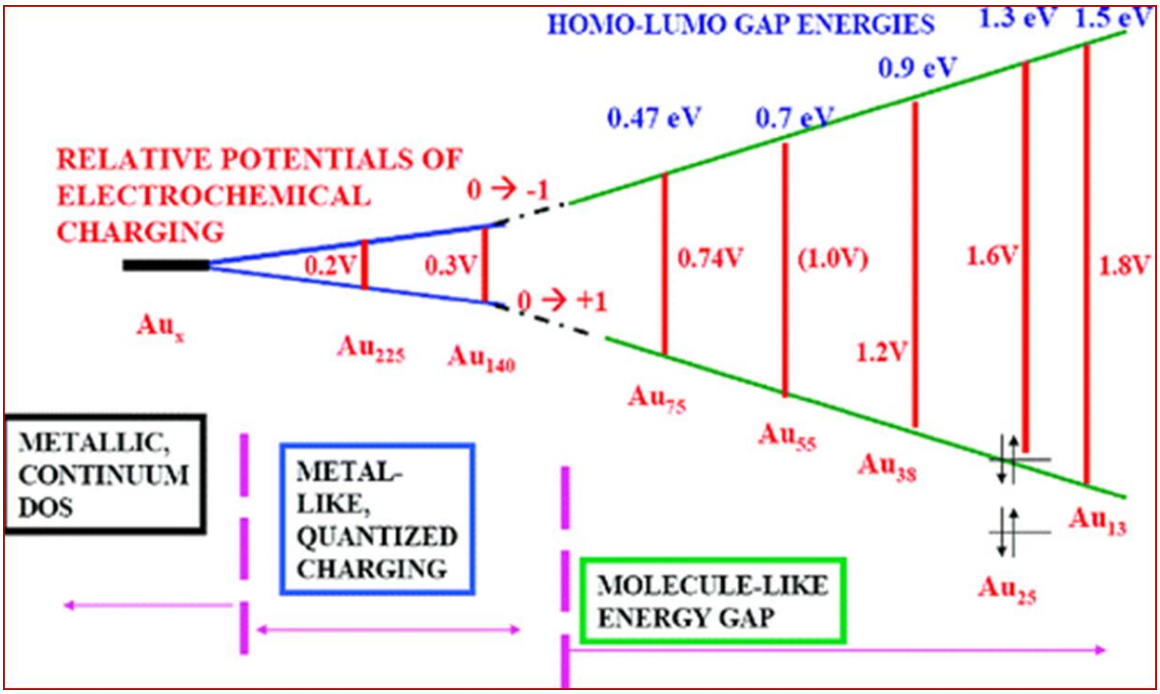

Figure 8. Summary of electrochemical behavior by MPC core size, showing estimated energy gaps (HOMO-LUMO gaps) and electrochemical energy gaps [image taken without permission from ref. 6].

Luminescence

Another defining optical characteristic for AuMPCs is its luminescent properties. AuMPCs less than two nanometers in diameter exhibit luminescence in both the visible and near-infrared (NIR) range. The wavelength of NIR luminescence for AuMPCs with gold core compositions of less than 200 atoms is not dependent on core size.[53] NIR luminescence intensities have also been found to increase linearly with proportion of polar thiolate ligands on the monolayer surface.[54] Further evidence indicates that the NIR luminescence emission of AuMPCs occurs from excited states located near the nanocluster surface.[55] More recent reports indicate that the interfacial

bond structure and the nature of the ligand play an important role in NIR fluorescence emission.[32,56-58] A model has been proposed for $Au_{25}(SR)_{18}$ in which excitation arises from the Au core, while luminescence decay results from relaxation of the Au_{13} core states to S−Au−S−Au−S semi-ring states. Therefore, the higher energy visible emission is dependent on core size, while the NIR emission is resulted from the electronic transition from S-Au-S-Au-S semi-ring states (LUMO) back to the ground Au_{13} core states (HOMO) (Figure 9).[58]

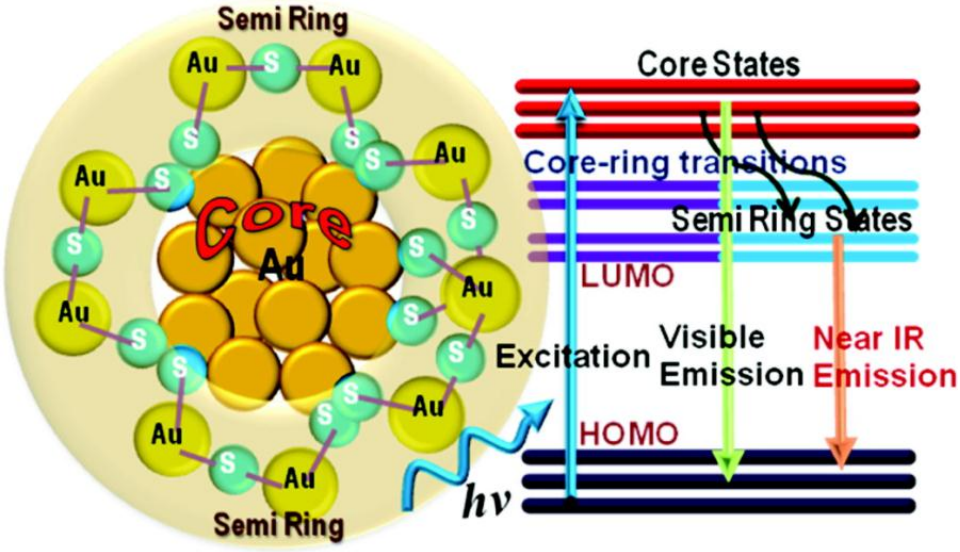

Figure 9. Cartoon diagram showing the relaxation pathways in $Au_{25}(SR)_{18}$ clusters [image taken without permission from ref. 58].

1.2.4 Other Methods of Characterization

In addition to being a reliable method for confirming the purity of the sample, nuclear magnetic resonance (NMR) spectroscopy is a particularly useful technique for AuMPC characterization. One well known ^{1}H-NMR characteristic of AuMPCs is the line-broadening effect, which is caused by motion restriction incurred on ligand protons by the rigid interfacial bond structure. Motion is heavily restricted for protons closest in proximity to the thiolate-gold interface, causing faster T_2 spin relaxation and broader peak shapes. Signals are less broadened

for protons on the ligand tails, which experience more freedom and range of motion.[37] 2D-NMR methods can also be used to estimate the size of AuMPCs in a monodispersed solution. Diffusion-ordered NMR spectroscopy (DOSY) was used to determine the diffusion coefficients of various gold nanocluster species, which by the Stokes-Einstein relationship can be applied to calculate the effective Bohr radii of each cluster.[32,59]

Many other methods are used to characterize AuMPCs. X-ray photoelectron spectroscopy (XPS) is a valuable tool for confirming the oxidation state of gold in the sample, based on the Au-Au and Au-S binding energies. Various imaging techniques are widely employed to determine nanoparticle size and sample dispersity, such as transmission electron microscopy (TEM)[27] and atomic force microscopy (AFM).[60] AuMPC composition is best resolved by high-resolution mass spectrometry (MS). The most widely used ionization methods for AuMPC characterization by MS are matrix-assisted laser desorption ionization (MALDI) and electrospray ionization (ESI).[49,61-63]

1.2.5 Applications of AuMPCs

The versatility of AuMPC application has attracted the attention of researchers from various disciplines. Larger AuMPCs (> 2 nm) can be exploited for biosensory applications based on surface plasmon resonance.[64-66] Scientists have extensively studied the possible roles of gold nanoclusters in new technologies for energy conversion. For example, gold nanoclusters have been utilized to serve as charge-transfer mediators for semiconductor-based photovoltaic devices.[67] Additionally, AuMPCs have been found to exhibit high catalytic activities for the catalysis of various reactions important for fuel cell implementation, such as methanol oxidation[68] and oxygen reduction.[47,69-73] AuMPCs have also shown great potential for application in green chemistry as new types of catalysts for organic synthesis[47,74-77] and CO oxidation.[47,78-84]

1.3 Silver Nanoclusters

Silver is the second-most studied metal nanoparticle behind gold, due to the ease of silver nanoparticle oxidation by reacting with atmospheric oxygen, leading to decomposition of the nanoparticles.[85] Non-thiolate ligands such as carboxylates,[13,85,86] amines,[87] and dendrimers[26,88] have been used to stabilize silver nanoparticles and nanoclusters with wide size distributions. One dendrimer-based synthesis has been reported to stabilize very small silver nanoclusters with a narrow size distribution.[89]

1.3.1 Silver Nanoclusters Stabilized by Thiolates

The most monodispersed syntheses have been performed by using dithiolate ligands as stabilizers. Rao et al. recently reported the solid-state synthesis of a monodispersed species, whose composition was indicated by ESI-MS to be $Ag_9(H_2MSA)_7$, where H_2MSA = mercaptosuccinic acid. Unfortunately, the stability of $Ag_9(H_2MSA)_7$ is poor when dissolved in water, which severely hinders attempts made towards further characterization.[90] It is also arguable whether or not the ion peaks observed by ESI-MS for this species are indicative of the intact cluster in solution or ion fragments generated in the analysis chamber, as significant ESI fragmentation is observed for other monodispersed AgMPC species.[91,92]

Similar to AuMPCs, the absorption spectra for AgMPCs are unique to each cluster composition within a certain size range, while larger silver nanoparticles all display the SPR absorption band at ca. 411 nm.[90-97] Another reported AgMPC synthesis employed glutathiolate (GS) as the stabilizing ligand, resulting in a mixture of several AgMPCs, which were separated by polyacrylamide gel electrophoresis (PAGE).[97] By comparing the PAGE separation bands between the AgMPCs and AuMPCs of known composition synthesized by a similar route, an estimated Ag core size was established for each fraction. The onset of UV/Vis absorption for

each fraction was used to estimate each HOMO-LUMO band gap, and an inverse relationship was established between the magnitude of the band gap and the Ag core size (Figure 10).[97]

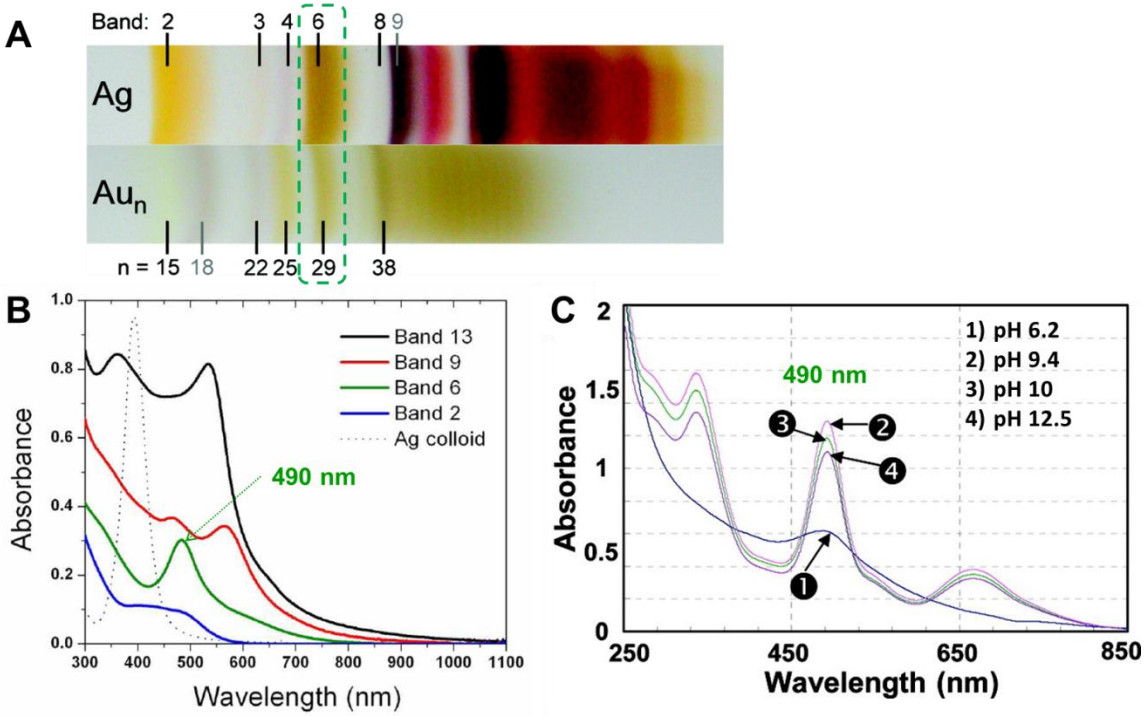

Figure 10. **(a)** PAGE separation for both $Ag_x(GS)_y$ and $Au_x(GS)_y$ mixtures. **(b)** Optical absorption spectrum for select fractions of $Ag_x(GS)_y$ from PAGE [images taken without permission from ref. 97]. **(c)** Absorption spectrum of monodispersed $Ag_x(GS)_y(CS)_z$ clusters with varying pH [image taken without permission from ref. 92].

Cathcart et al. recently reported the synthesis of monodispersed AgMPCs using a mixed monolayer of GS and captopril (CS) thiolate ligands.[92] The absorption spectrum for this species remarkably resembles that of fraction 6, sharing the same strong absorption peak at ca. 490 nm (2.5 eV) (Figure 10-B,C). The comparable patterning of the PAGE separation may indicate structural similarities between band 6 and its respective gold analogue, $Au_{29}(GS)_{20}$.[44,97] Unfortunately, no molecular ions could be resolved for the $Ag_x(GS)_y(CS)_z$ clusters by ESI-MS, only fragments $Ag_4L_4^-$ and $Ag_4L_3^-$.[92] Note that the absorption for the $Ag_x(GS)_y(CS)_z$ clusters is sensitive to pH, as more well-defined features are present at higher pH (Figure 10-C). The pH

sensitivity is hypothesized to be attributed to the function of the carboxylate groups on each thiolate ligand molecule, as discussed in Chapter 3.

Unlike AuMPCs, the luminescence emission for AgMPCs is usually only observed in the visible range,[90-92,97] with the exception of 4-fluorothiophenol (4-FTP) capped AgMPCs reported by Bakr et al., for which the emission maximum was centered at 1375 nm.[96] No X-ray crystal structure has yet been reported for an AgMPC, but it will be interesting to discover how the interfacial bond structure compares to the staple motif of AuMPCs and how such structural characteristics govern AgMPC energetics.

1.3.2 Silver Nanoclusters Stabilized by Dithiolates

One synthesis has been reported in literature for a monodispersed dithiolate-stabilized silver nanocluster (AgDTC) using dimercaptosuccinic acid (DMSA) as the ligand. The resulting species was given the composition $Ag_7(DMSA)_4$ using ESI-MS.[98] Contradicting this assignment is the absorption spectrum, which displays a well-defined peak at 500 nm, bearing a striking resemblance to band 6 in the PAGE separation, therefore corresponding to a larger core size. It is possible that the base peak observed in ESI-MS is actually a stable fragment ion of the larger cluster. But as was mentioned in the introduction of Chapter 1, the properties of AgDTCs cannot be predicted based on trends set by AgMPCs, so the MS assignment may be correct. The stability of this AgDTC is an issue which has hindered attempts at characterization.

1.4 Copper Nanoclusters

Reports of successful syntheses are more limited for copper nanoclusters, due to the relatively higher reactivity of copper versus gold and silver. Copper nanoparticles are easily prone to oxidation from atmospheric oxygen. Despite these drawbacks, researchers have made substantial progress in recent years. A remarkable example is the electrochemical synthesis of copper

nanoclusters with Cu_n, ($n \approx < 14$), stabilized only by tetrabutylammonium cation.[99] For this synthesis, however, the nanoclusters must be kept in solution with excess tetrabutylammonium salts to remain stable. Other wet chemical methods employing non-thiolate capping agents as stabilizers resulted in large copper nanoparticles exhibiting plasmonic properties.[17,100-105]

1.4.1 Copper Nanoclusters Stabilized by Thiolates

Thiolates have proven so far to be the best choice of ligand for producing stable copper nanoclusters, due to the strong covalent nature of the Cu-S interaction.[24] Monothiolates have been used to synthesize stable CuMPCs, with some reported clusters being of relatively large size (> 2 nm in diameter).[106] Other CuMPC syntheses have resulted in smaller, more stable clusters (< 2 nm in diameter).[107-110] Quantized double-layer charging has been observed for CuMPCs,[107] as well as luminescence in the visible range.[110] Much more has yet to be accomplished in CuMPC research, as there are no known reports for the synthesis and characterization of a monodispersed sample. The synthesis of copper nanoclusters by using dithiolate ligands has not been reported by a previous group.

1.4.2 Potential Applications of Copper Nanoclusters

The reactivity of elemental copper gives credence to the potential utilization of copper nanoclusters as catalysts. In organic synthesis, copper nanoparticles have been exploited as useful catalysts for various click chemistry reactions.[111,112] Efficient catalysis of selective Michael addition reactions has been achieved using copper nanoparticles in ionic liquid.[113] Dispersions of copper nanoparticles on semiconductor surfaces have proven effective in catalyzing the water-gas shift reaction for oxidation of carbon monoxide.[114] In a recent paper, CuMPCs have shown electrocatalytic activity in the oxygen reduction reaction (ORR).[110] Catalytically active copper nanoclusters are a much more cost-effective alternative to the

currently used platinum-based catalysts for ORR in fuel cell applications. The development of such affordable catalysts could lead to the realization of fuel cells as economically feasible alternatives to the combustion of fossil fuels.

1.5 Research Aims: Metal Nanoclusters Stabilized by Dithiolates

To create nanoclusters with novel properties, the primary method of synthesis investigated by our group involves the use of dithiolates as protecting ligands. The dithiolates are proposed to have advantages over the more commonly used monothiolates due to the chelate effect, resulting in clusters with enhanced stability.[21] Little progress has been made in understanding the structure and properties of dithiolate-protected clusters (DTCs), although metal nanoparticle syntheses have previously proven successful by employing dithiols as stabilizing ligands.[32,115-118] It is hypothesized that the structure and properties of the chosen dithiolate ligand plays a substantial role in the unique energetics for the resulting DTCs. Described herein is the investigation into new gold, silver, and copper nanocluster species stabilized by dithiolates with an emphasis on optical and electrochemical characteristics.

2. ENERGETIC PROFILE OF MIXED THIOLATE GOLD CLUSTERS

2.1 Introduction

A gold mixed-thiolate protected cluster (AuMTC) was synthesized in our group by employing a mixture of durenedithiolate (durene-DT) and phenylethanethiolate (PhC_2S) as the stabilizing ligands. The average composition for these clusters was characterized to be Au_{130}(durene-DT)$_{29}$(PhC_2S)$_{22}$ by mass spectrometry, H-NMR spectroscopy, and thermogravimetric analysis.[119] Electrochemical methods were used to elucidate the energetics of the AuMTC. An energy diagram is proposed, correlating the optical and electrochemical properties. The AuMTC properties do not fit in with the core size trend established by AuMPCs. While they do display some properties that would be expected based on AuMPC research, e.g. quantized double layer charging, they also exhibit rich optical features, not previously observed for AuMPCs of such size.

2.2 Results and Discussion

2.2.1 Electrochemistry of Au_{130}MTCs

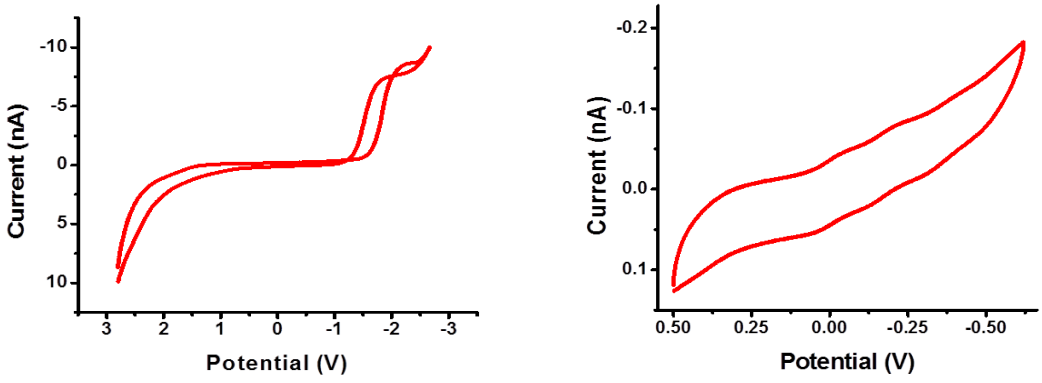

Figure 11. Cyclic voltammograms of the Au_{130} MTCs in DCM with 0.1 M TBAP, measurements were taken at low temperature (-70 °C) and 100 mV/s scan rate.

Cyclic voltammograms (CVs) (Figure 11) and square wave voltammograms (SWVs) shown in Figure 12 were collected at low temperature for better peak resolution at broad potential window. Precise peak potentials were measured by differentiating the data and extrapolating the derivative plot to cross zero (Figure 13). Those values corresponding to the notable SWV peaks were listed in Table 1 for the calculation of electrochemical energetics. Four uniformly spaced peaks (#2-5) near zero potential can be clearly seen in panel B of Figure 12. This corresponds to continuous quantized charging of two degenerated energy states. A differential pulse voltammogram at room temperature is provided in Figure 14, clearly showing the uniform peak spacing between each of the four peaks.

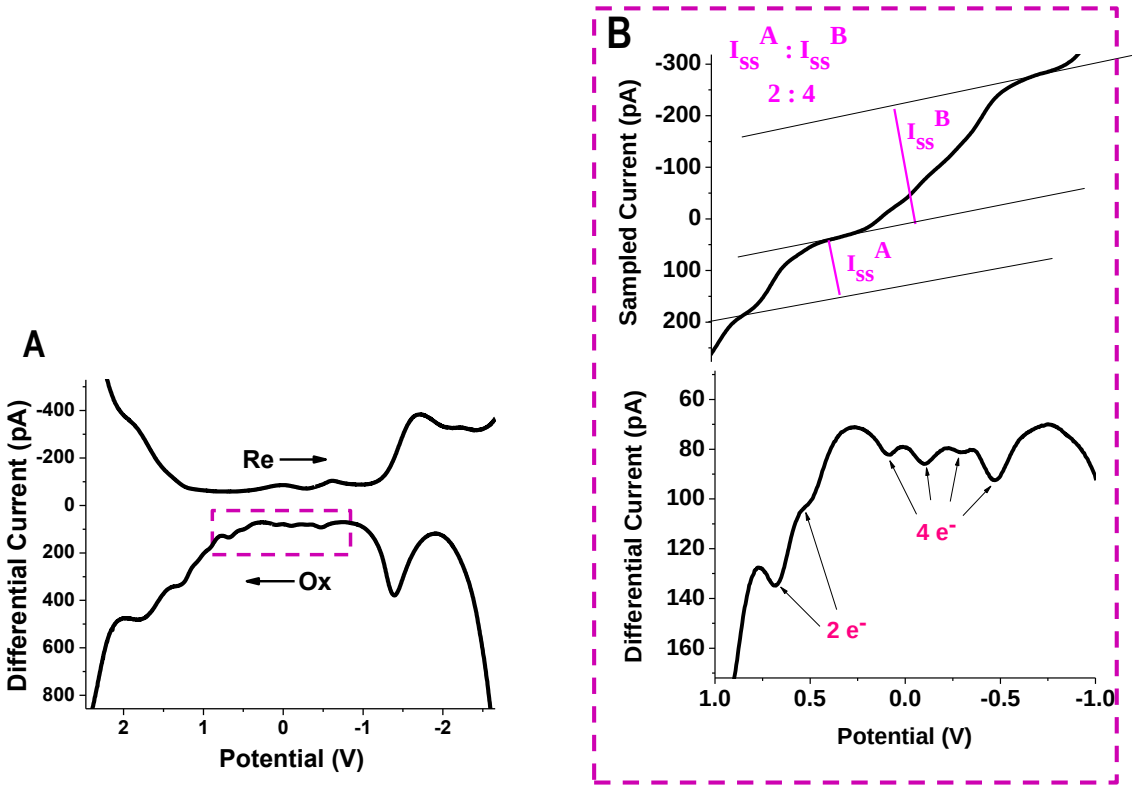

Figure 12. (a) Square wave voltammogram (SWV) of AuMTCs, recorded in 0.1 M TBAP in DCM solvent at -70°C. **(b)** Zoom in of oxidation scan in SWV with one corresponding sampled current shown above. Step amplitude was at 25 mV with 4 mV increments. Frequency was 15 Hz.

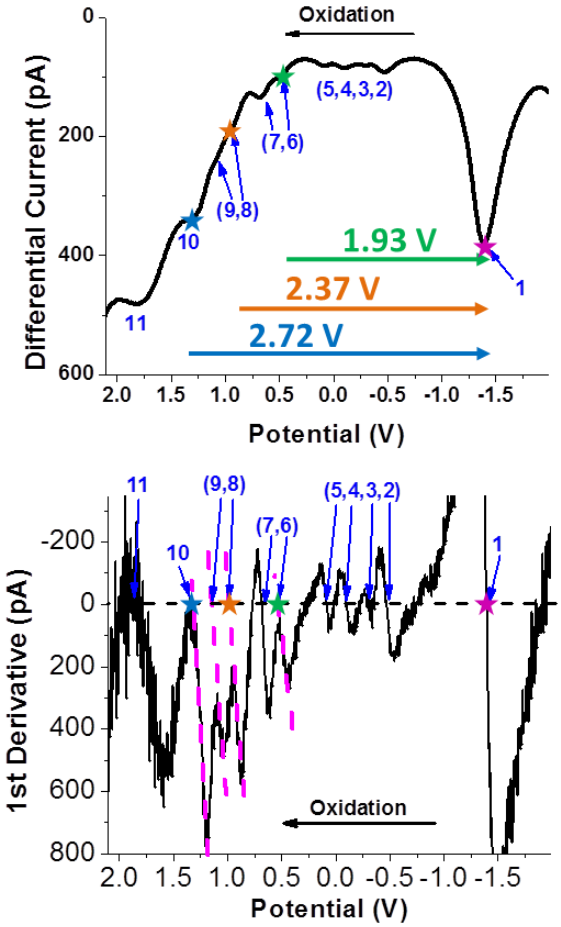

Figure 13. SWV oxidation scan of the Au_{130} MTCs from Figure 6 with 1st derivative plot shown in bottom panel. Stars indicate peaks used for optical correlation.

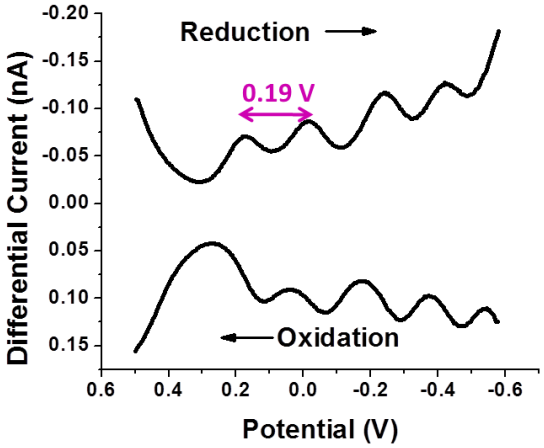

Figure 14. Differential pulse voltammogram of the Au130 MTCs in DCM with 0.1 M TBAP, measurement was taken at narrow potential range, room temperature.

Table 1. Formal potential spacings for the AuMTCs, data calculated from Figure 13.

Peak #	**11**	**10**	**9**	**8**	**7**	**6**	**5**	**4**	**3**	**2**	**1**
Potential (V)	**1.84**	**1.32**	**1.14**	**0.97**	**0.68**	**0.53**	**0.09**	**-0.10**	**-0.30**	**-0.47**	**-1.40**
Peak spacing	**11-10**	**10-9**	**9-8**	**8-7**	**7-6**	**6-5**	**5-4**	**4-3**	**3-2**	**2-1**	
Energy (V)	**0.52**	**0.18**	**0.17**	**0.29**	**0.15**	**0.44**	**0.19**	**0.20**	**0.17**	**0.93**	

Recall from Chapter 1 that continuous quantized charging behaviors have been observed from large AuMPCs such as $Au_{144}(SR)_{60}$,[16,17] in contrast to smaller clusters such as $Au_{25}(SR)_{18}$ that display electron transfer (ET) activities at discrete energy states.[18] Au_{130} MTCs exhibit unique electrochemical behaviors that set them apart from either category. The charging energy of Au_{130}MTCs is determined by the average peak spacing at 0.19 V. This value is slightly smaller than that observed in PhC_2S and hexanethiolate stabilized MPCs.[15,16] Durene-DT has one instead of two methylene groups between the Au core and benzene ring in contrast to PhC_2S, therefore slightly less monolayer thickness and larger dielectric constant, which leads to smaller charging energy. Separated by a 0.44 V gap (peak # 6-5), another pair of ET peaks reveals one energy state below the two degenerated states. The current ratio is found to be 2:4 from one scan of the square wave data (comparable to CV current). Therefore, all six differential current peaks are attributed to single electron transfer activities. The baseline distortion in sampling current prohibits similar interpretation at higher potentials where more electron transfers occur.

2.2.2 Correlation of Electrochemical and Optical Energetics

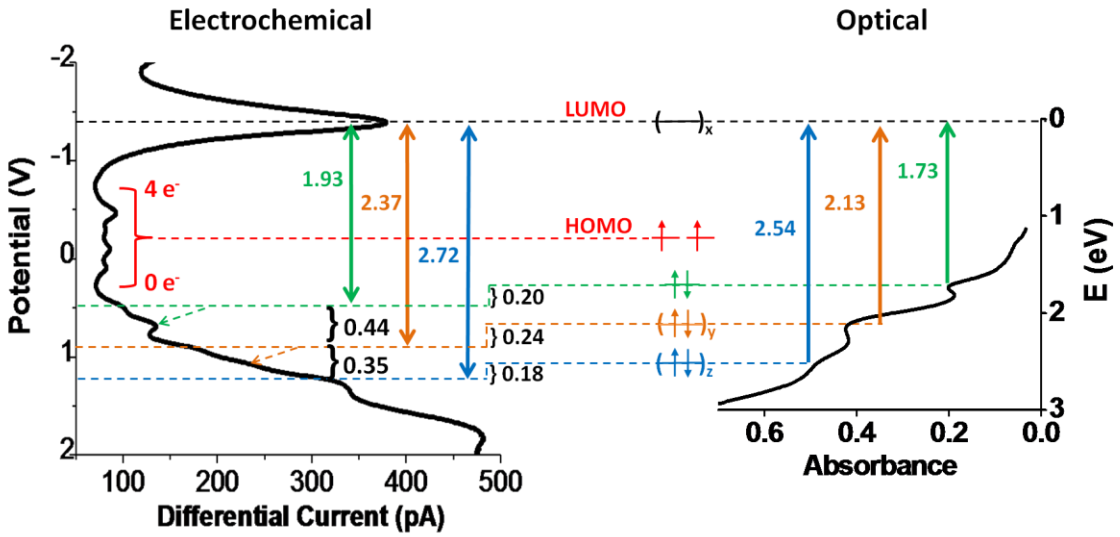

Figure 15. Energy diagram that correlates optical and electrochemical features. The SWV oxidation scan *(left)* and absorbance spectrum *(right)* are aligned based on the energy states shown in the middle. The undetermined degeneracy of those states are denoted x, y and z.

Each UV-Visible absorption peak is a result of photon-induced electronic transitions from lower to higher energy states, and thus should also correlate to observed electrochemical band gaps. Oxidation scan generally offers better resolved features compared to reduction scan, presumably due to the impacts on Au-thiolate bonding by reduction. This is supported by the cyclic voltammetry in Figure 11, in which the high potential peaks are found to be irreversible and significantly distorted. Shown in Figure 15, excellent match is established between optical bands and respective electrochemical gaps.

Starting from the molecular orbital diagram at the center, two degenerated HOMO orbitals could hold 0-4 electrons (two shown), generating four continuous ET peaks separated by charging energy. Interestingly, a single dominant ET peak at -1.4 V is observed upon reduction, suggesting common LUMO states. With the distinct LUMO as reference point, electrochemical and optical transitions are correlated. The first three optical absorption bands at 1.73, 2.13 and

2.54 eV are matched with corresponding electrochemical peaks as indicated. Note the first of the two ET peaks in each energy state (corresponding to 1.73 and 2.13 optical bands) is used in the comparison. The second electron transfers per orbital are indicated by the arrow, requiring additional charging energy compared to the initial ET. The average differences between measured optical and electrochemical transitions (0.20 V) are approximately equivalent to the measured charging energy (0.19 V). The high background signal at high potentials and potential structure/composition changes of MTC at high charge states in electrochemistry prohibit the precise correlation of the 3.50 eV optical band, as well as the degeneracy of those energy states indicated by x, y and z.

The HOMO-LUMO band gap is extrapolated to be ca. 0.88 eV from the absorption spectrum, but varies from sample to sample and is not as well-defined as the other bands. For an ideal neutral MTC sample, the HOMO-LUMO gap is predicted to be 0.74 V from electrochemistry, calculated from the gap between the LUMO peak and the last charging peak of the HOMO (0.93 V) with one charging energy value (0.19 V) subtracted. With several electrons filling the degenerate HOMO states, the Fermi level will shift accordingly, which will cause the apparent optical band gap to fluctuate. Indeed, the rest potential of the sample used here is ~0.2 V with Ag/AgCl wire as quasi reference electrode. Precise control of the rest potential by bulk electrolysis methods is currently underway.

2.2.3 Electrochemistry of Durene-DT Ligand

The free durene-DT alone displays electrochemical behavior at negative potential. This was found to be a one-electron reduction by comparing the CV current response to that of an equimolar solution of ferrocene (Figure 16). Since the electrochemical reduction of benzene to 1,3-cyclohexadiene involves a two-electron reduction,[120] the one-electron reduction behavior

was attributed to the formation of an intramolecular anionic cyclic disulfide radical. Radical disulfide anions on six-membered rings have been detected previously for dithiothreitol by EPR spectroscopy.[121,122] Durene-DT is reduced at -1.81 V to durene-disulfide radical anion, which is then oxidized in the reverse scan to durene-disulfide at -1.67 V (Figure 16).

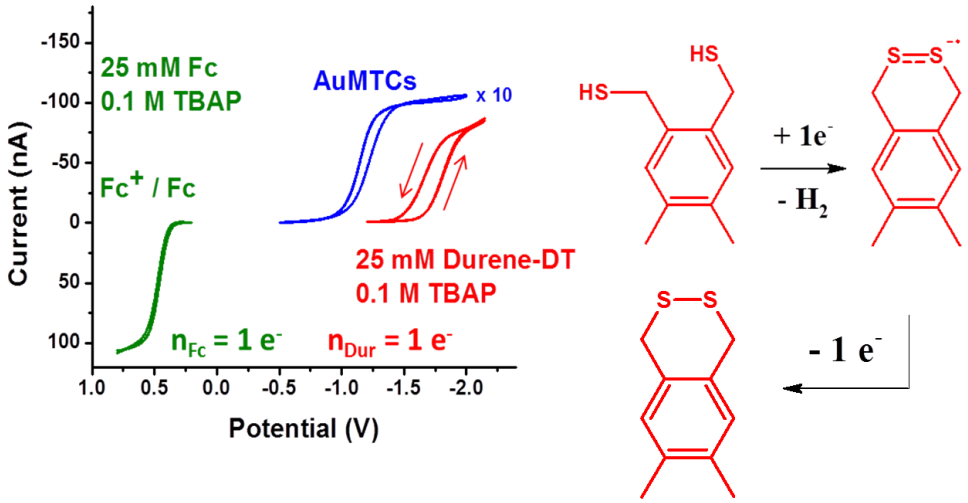

Figure 16. (a) Cyclic voltammograms of ***(green)*** 25 mM ferrocene, ***(red)*** 25 mM durene-DT, and ***(blue)*** reduction peak for AuMTCs (data scaled by factor of ten for clarity). All scans were performed with 0.1 M TBAP supporting electrolyte in DCM and 100 mV/s scan rate, Pt disk working electrode (7.4 µm). CV of AuMTCs was recorded at ca. -70°C in dry ice/acetone bath. **(b)** Structural representation of durene-DT reduction to durene-disulfide radical anion and oxidation to durene-disulfide.

The electrochemical response from the LUMO of AuMTCs, however, is not the same as that of durene-DT alone, as the latter occurs at more negative potentials (higher energy). This suggests that the electrons being transferred are much more stable in the form of durene-DT that is attached to the AuMTC. It is therefore proposed that the electrons are being conducted through the delocalized disulfide radicals to charge the Au core. The conduction of charge through the ligands effectively increases the dielectric constant for the compact layer of the AuMTC, resulting in the overall substantial increase of the quantum double layer capacitance and decrease in ΔV, following Equation 1 provided in Chapter 1. The charging energy then becomes

negligible (i.e. no longer discernable by voltammetry), as no peak separation is observed between each ET at the LUMO potential (-1.4 V). Such behavior has never been observed before, as previously reported AuMPC voltammograms all display relatively regular potential difference spacings between ET peaks, regardless of corresponding energy level.[40-47] However, as mentioned earlier, the regular charging phenomena still exists for the electron transfers at the HOMO and more positive potentials (Figures 12-14). At these potentials the AuMTCs behave "normally," i.e. the attached durene-DT ligands no longer serve as conductors, so the typical capacitive effects of the compact layer are still present.

2.2.4 Metal to Ligand Charge Transfer Quantization

Since there are multiple durene-DT ligands attached on the monolayer of an AuMTC, the amount of charge transferred to each conducting ligand cannot be determined by direct comparison of steady state current from voltammetry, as was used for the peaks at positive potential in Section 2.2.1 (Figure 12-B). However, if each attached durene-DT is treated as a redox-active analyte, then the quantification of ET per attached durene-DT molecule can be achieved by comparing the relative scan rate dependence in cyclic voltammetry, according to Equation 2:[123]

$$\mathbf{i_p = (2.69 \times 10^5) n^{3/2} A D^{1/2} C \nu^{1/2}} \qquad \mathbf{(2)}$$

i_p = peak current, n = # of electrons transferred, A = area of working electrode,
D = diffusion coefficient, C = concentration, ν = scan rate

The radius of the disk electrode used in these measurements is 7.4 μm. For a nanoelectrode of this particular size, which lies in the transition from microelectrode to ultramicroelectrode, the kinetics of mass-transfer can be described by either radial diffusion or linear diffusion, depending on the scan rate used. Shown in Figure 17 is the measured peak current from CV vs.

the square root of the scan rate for the single electron transfer at QDL peak 2 (Table 1). The transition from diffusion-limited current response to steady-state response is clearly evidenced by the change from a steep slope at high scan rates to an almost flattened slope at lower scan rate.

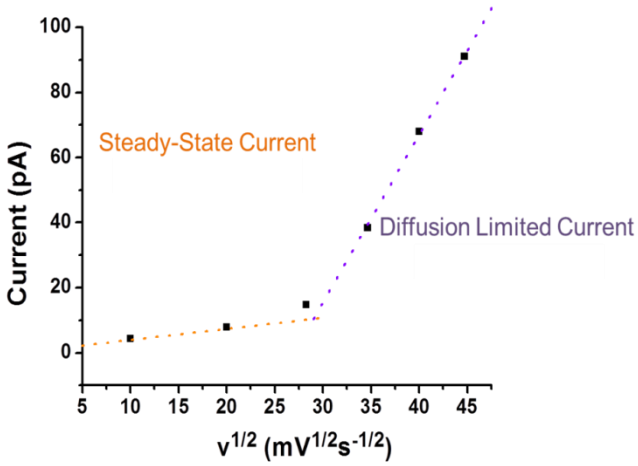

Figure 17. Plot of peak currents measured from CV versus square root of the scan rate for QDL peak 2.

Based on this finding, the CV current responses at high scan rates were analyzed. As shown in Figure 18, the scan rate dependence for both the Au QDL peak and the durene-DT peak were determined from the linear fit of their respective i_p vs. $v^{1/2}$ plots. Since the values of A, D, and C are all equivalent, the following relationship can be established based on Equation 2:

$$\mathbf{i_{QDL}(n_{QDL})^{-3/2} v^{-1/2} = i_{Dur}(n_{Dur})^{-3/2} v^{-1/2}} \quad \mathbf{(3)}$$

Substituting the slope, k, for $i / v^{1/2}$ gives:

$$\mathbf{k_{QDL}(n_{QDL})^{-3/2} = k_{Dur}(n_{Dur})^{-3/2}} \quad \mathbf{(4)}$$

And since $n_{QDL} = 1\ e^-$, the expression is even further simplified as:

$$\mathbf{k_{QDL}(n_{QDL})^{-3/2} = k_{Dur}} \quad \mathbf{(5)}$$

The slope values from Figure 18 were then used to solve for an n_{Dur} value of 4 e^-. Assuming each durene-DT ligand on the cluster is acting as a conducting ligand, for the composition

$Au_{130}(Durene\text{-}DT)_{29}(PhC_2S)_{22}$, a total of 116 electrons would be charged into the Au_{130} core at the potential of -1.4 V. This is impossible because the steady state current ratio of $i_{ss}^{Dur} : i_{ss}^{QDL}$ from SWV is 48:1, which cannot occur if all 29 durene-DT ligands are activated (Table 2). Therefore the n_{Dur} value of 4 e^- can only be correct if a fraction of the total durene-DT ligands are participating in charge transfer. This is reasonable since the steady state current of the durene-DT response varies from sample to sample. Following this logic, a total of 12 durene-DT ligands are calculated as participants in 4e^- charge transfer for this particular sample.

Table 2. Comparison of Steady State Current from SWVox in Figure 12.

	Durene-DT Peak	4 QDL Peaks
Potential (V)	**-1.40**	**(0.09, -0.10, -0.30, -0.47)**
i_{ss} (pA)	**1288**	**108**
$i_{ss}^{Dur} : i_{ss}^{QDL(total)}$	**12 : 1**	
$i_{ss}^{Dur} : i_{ss}^{QDL(individual)}$	**48 : 1**	

The n_{Dur} value may also be in error, since the H-NMR of the sample used in this analysis still displays a significant degree of sharp durene-DT proton signals in relation to the broadened peaks, suggesting free durene-DT is present in the sample or a small complex. In either case the presence of another component that is also electroactive at -1.4 V significantly complicates the analysis, such that the diffusion coefficients and concentrations can no longer be treated as equivalent in Equation 2. Instead the current for attached durene-DT appears to be much larger than it really is. In relation, the calculated n_{Dur} in this experiment might be much larger than the real value. If the value of n_{Dur} is actually 1e^-, agreeing with the results from Section 2.2.3, then a total of 48 charge transfer active durene-DT ligands is suggested from Table 2. This value is somewhat larger than the accepted composition of 29 durene-DT ligands, which can be explained by the presence of free durene-DT or durene disulfide in the sample. Following that

each charge transfer is $1e^-$, it is proposed that all of the attached durene-DT ligands are participating in charge transfer.

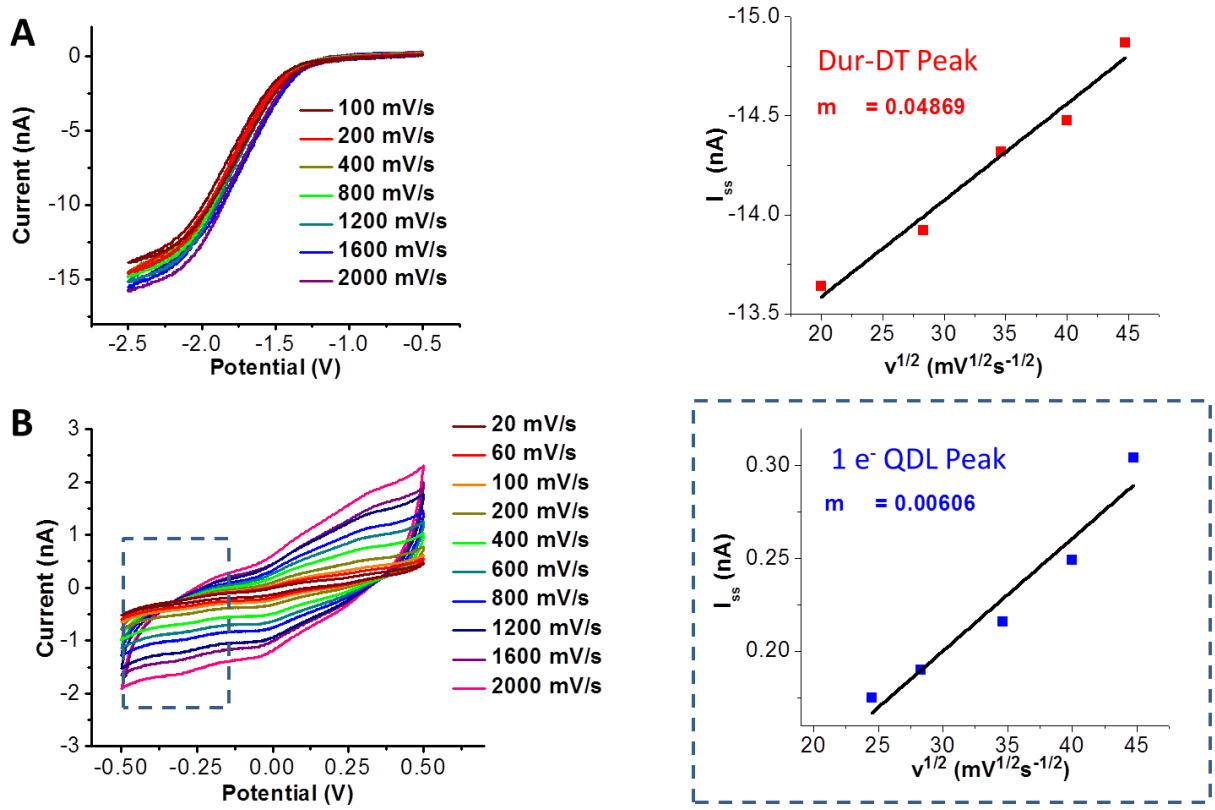

Figure 18. (a) CVs at various scan rates for LUMO peak with corresponding i_p vs. $v^{1/2}$ plot. **(b)** CVs at various scan rates for QDL peak 2 of AuMTCs collect at RT with corresponding i_p vs. $v^{1/2}$ plot. The linear fit and corresponding slope, m, is also shown. CVs were recorded using 7.4 μm Pt electrode in DCM with 0.1 M TBAP supporting electrolyte.

2.3 Conclusions

The electrochemical behavior of $Au_{130}(Durene\text{-}DT)_{29}(PhC_2S)_{22}$ has been characterized and energetics correlated to the absorption spectrum. At negative charge states (negative applied potential), the attached durene-DT ligand is transformed into a delocalized radical species which serves to conduct electrons into the gold core. While the methods used to quantify charge transfer of the attached durene-DT ligand are correct, the results are not reliable due to the presence of free durene-DT or durenedisulfide as evidenced by H-NMR. Since only one electron

transfer occurs for free durene-DT at ca. -1.6, it is predicted that just one electron is transferred per attached durene-DT on the MTC surface. To test this hypothesis correctly in the future, the AuMTC sample must be pure. A more pure sample is also necessary to confirm the proposed optical and electrochemical correlation. Experiments are currently underway to sufficiently elucidate this unique charge transfer behavior.

3. SILVER DITHIOLATE-STABILIZED NANOCLUSTERS

3.1 Introduction

One synthesis has been reported in literature for a monodispersed dithiolate-stabilized silver nanocluster (AgDTC) using dimercaptosuccinic acid (DMSA) as the ligand. The resulting species was given the composition $Ag_7(DMSA)_4$ using ESI-MS.[98] Contradicting this assignment is the absorption spectrum, which displays a well-defined peak at 500 nm, bearing a striking resemblance to band 6 in the PAGE separation, therefore corresponding to a larger core size. It is possible that the base peak observed in ESI-MS is actually a stable fragment ion of the larger cluster. But as was mentioned in the introduction of Chapter 1, the properties of AgDTCs cannot be predicted based on trends set by AgMPCs. The stability of this AgDTC is an issue which has hindered attempts at characterization, a problem shared by the newly reported AgDTC discussed below, which features lipoic acid (LA), a 1,3-substituted disulfide.

3.2 Synthesis

AgDTCs were synthesized by a one-phase method in aqueous solvent under basic conditions (Figure 19). Briefly, lipoic acid in 25 mM NaOH solution was used to dissolve silver nitrate by sonication, forming a pale yellow solution. Next, a solution of sodium borohydride in 25 mM NaOH was added. The color of the reaction mixture gradually changed from yellow to dark red. After reduction the reaction mixture was stirred for twelve hours to allow the clusters to evolve from a polydispersed to a monodispersed sample, as monitored by UV/Vis absorption.

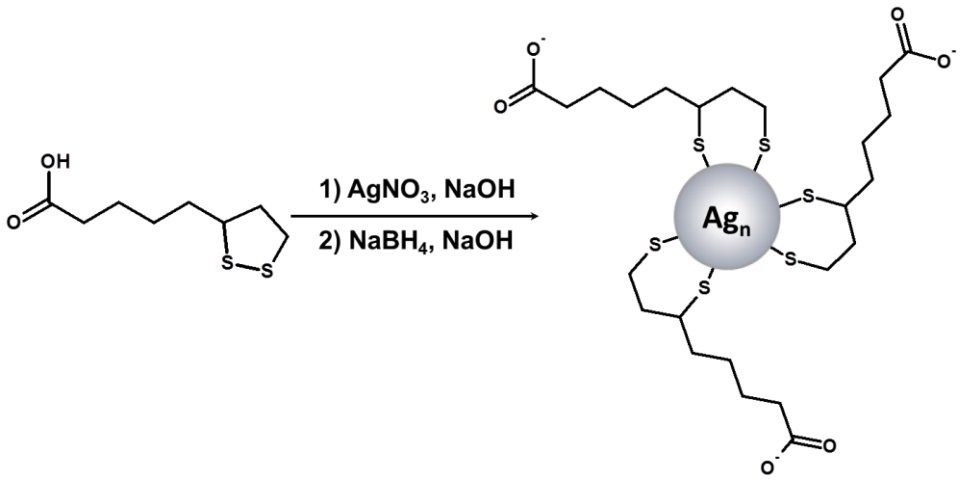

Figure 19. Synthetic scheme for LA-AgDTCs. Cartoon of cluster is not drawn to scale or indicative of composition.

3.3 Results and Discussion

The rich defined features in the absorbance spectrum of the AgDTCs indicate that the most thermodynamically favored species was synthesized (Figure 20). Four absorbance peaks are clearly visible at 4.77 eV, 3.73 eV, 2.90 eV, and 2.47 eV. The HOMO-LUMO band gap is estimated from the band edge at ca. 2.0 eV. This band edge is very close in value to that reported by Kumar, et al. for a species proposed to have a core composition of Ag_{15}.[97] If the pH is brought below pH 8 the clusters appear to become more polydispersed with larger clusters formed (Figure 21). This effect is analogous to that observed for the AgMPCs stabilized by glutathione/captopril, as described in Section 1.3.1.[91,92] The clusters also exhibit strong red fluorescence emission with only one maximum centered at ca. 645 nm, another property shared with AgMPCs of diameter less than 2 nm.[90-92,95]

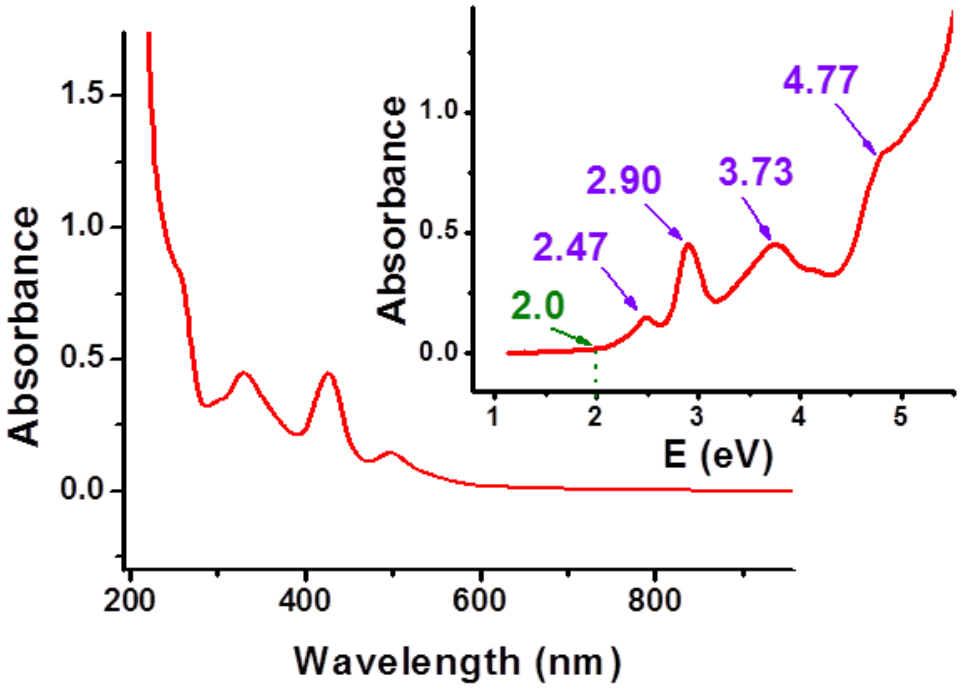

Figure 20. Optical absorption spectrum for as-synthesized AgDTCs. Inner panel shows absorption plotted on energy axis and labeled peak energies. Green label points to the absorption band edge.

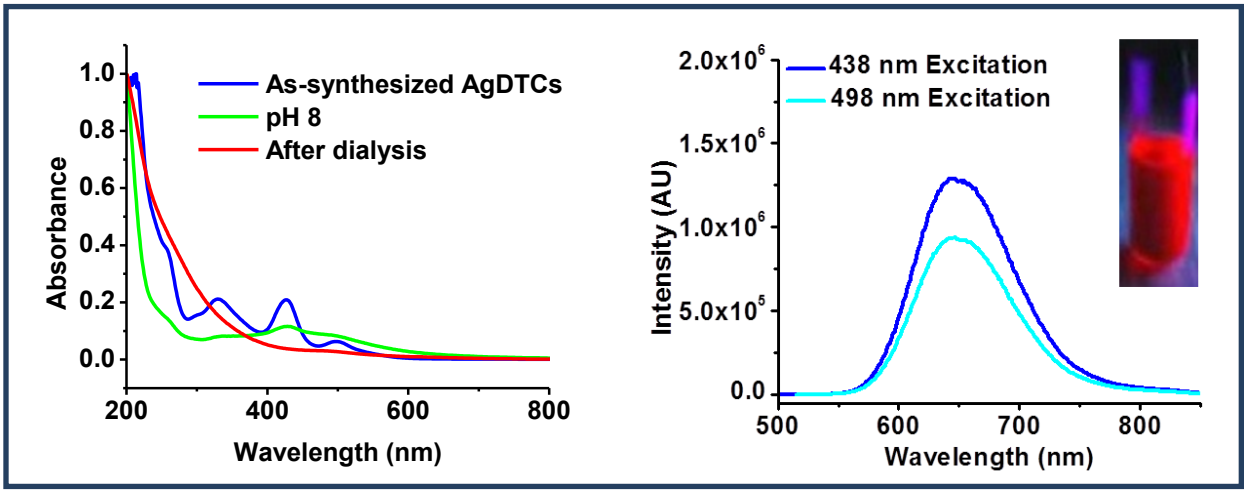

Figure 21. (left panel) UV/Vis absorption spectrum of 2X-LA-Ag synthesis, pH effect, and purification. (right panel) Fluorescence spectra of LA-AgDTCs in NaOH solution, 3 nm slitwidth with photograph of LA-AgDTCs under UV lamp radiation.

The unpurified AgDTC sample can maintain its optical features for several weeks in alkali solution under ambient conditions. Since the carboxylate groups on the tails of the attached ligands are negatively charged at pH > 8, the clusters can be transferred to the organic phase via TOA cation. The efficiency of this transfer is poor, since there is a great excess of competing Na^+ in the system. The absorption spectrum of the AgDTCs in organic solvent is virtually identical to that observed in water (Figure 22).

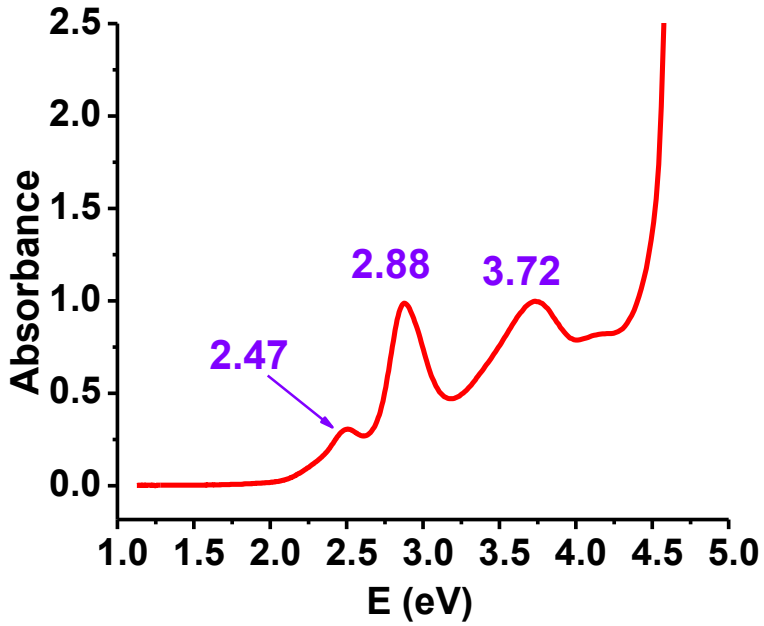

Figure 22. Optical absorption spectrum for AgDTCs in dichloromethane after phase transfer with tetraoctylammonium bromide.

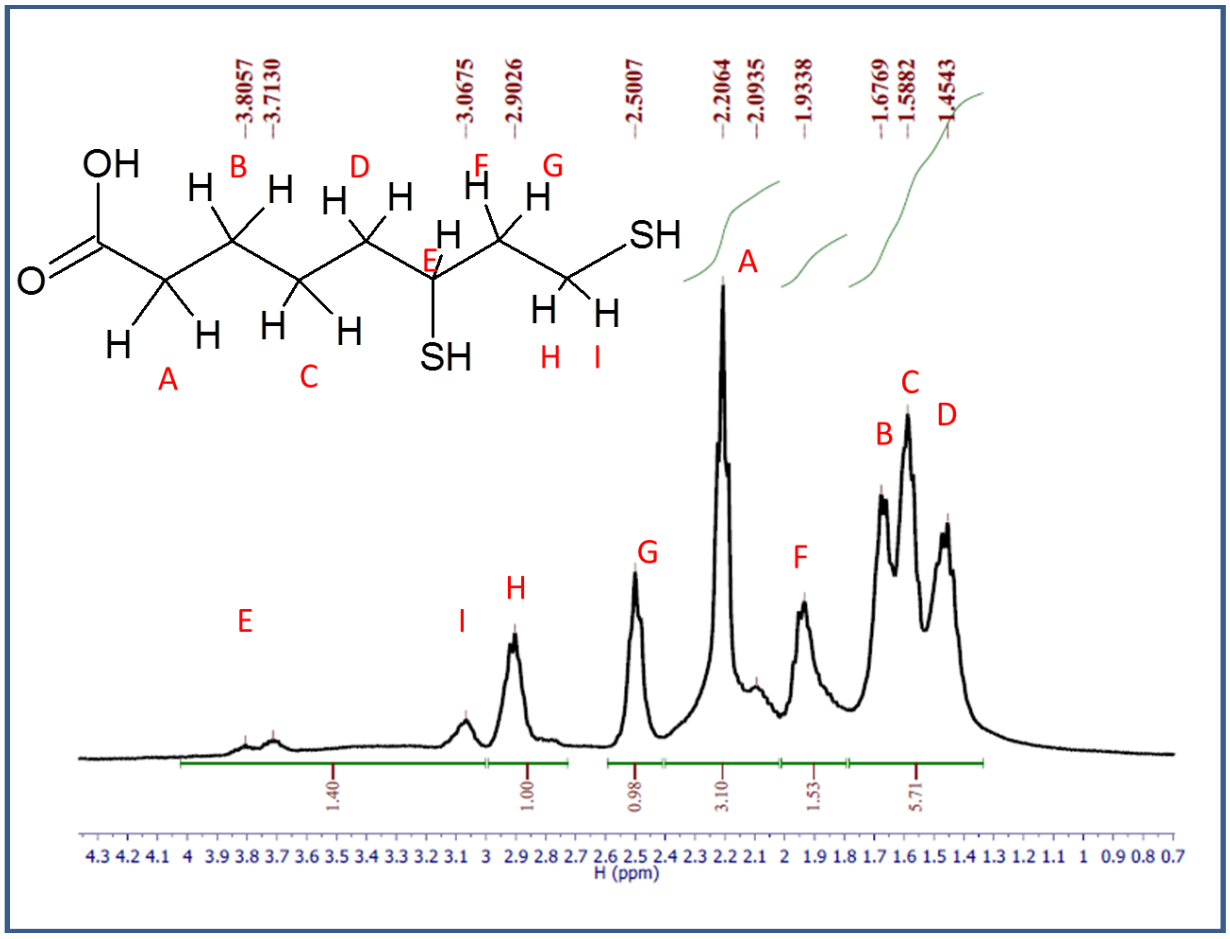

Figure 23. H-NMR Spectrum for LA AgDTCs in D_2O solvent. Structure of dihydrolipoic acid shown in top left corner.

The altered product after dialysis purification can still be dissolved in water, and was analyzed by NMR spectroscopy (Figure 23). The H-NMR spectrum of the lipoic acid silver clusters shows signal broadening effects, indicating ligand attachment to a silver nanocluster. Broadening is much more obvious for the proton signals downfield, which pertain to the protons closest to the thiolate and silver core. Sharper signals are observed for the protons neighboring the carboxyl group on the ligand tail, located furthest away from the point of attachment to the metal core. It is suggested by the H-NMR evidence that AgDTCs still survive the purification, yet aggregate and form larger particles, creating a polydispersed size distribution, as suggested by the UV/Vis absorption spectrum (Figure 21-red line).

3.4 Conclusions

Nanocluster synthesis under basic conditions with LA ligand results in a monodispersed, yet pH sensitive AgDTC sample. The cluster exhibits intense fluorescence and well-defined absorbance features. The negatively charged AgDTCs can be transferred to the organic phase by quaternary ammonium salt. An anhydrous synthesis in organic phase is therefore feasible using quaternary ammonium cation instead of sodium cation as the charge stabilizer, resulting in DTCs that are more stable. Investigations into the anhydrous synthesis of LA-AgDTCs in organic solvent are currently underway. If the aqueous AgDTCs are to be successfully purified, the pH must be controlled at pH > 10 by using a buffer compatible with ESI-MS, such as Tris. The dialysis tube and chamber can both be comprised of the buffer, maintaining a constant pH during purification. All characterization must include the buffer to keep the clusters stable. Regardless of the means used to synthesize and purify these AgDTCs, a mass spectrum is necessary for compositional characterization. ESI-MS experiments are currently in progress. Also necessary are IR spectroscopy and/or H-NMR in organic solvent to determine whether or not there are any thiol groups still present in the sample. Quantum efficiency should also be calculated for the brilliant fluorescence emissions from these DTCs.

4. COPPER DITHIOLATE-STABILIZED CLUSTERS

4.1 Introduction

While much research has been focused on the synthesis, characterization, and applications of noble metal nanoclusters (primarily gold), little improvement has been achieved with low cost metals such as copper. Advancing research into the realm of copper may lead to the discovery of exciting new cost-effective catalysts for energy conversion technologies such as fuel cells and photovoltaics or green chemistry applications such as organic synthesis and catalytic conversion of carbon monoxide.[113,114]

The major reason why research is lacking for monolayer-protected copper nanoparticles is the high reactivity of copper with oxygen, forming oxides which contaminate the sample and compromise stability.[124] Dithiol ligands are expected to enhance the overall stability of the cluster by entropy gain and prevent oxidation and decomposition of the copper nanoparticles. Furthermore, the high stability of the dithiolate-Cu bond structure is proposed to aid in the synthesis of monodispersed relatively small copper dithiolate-protected nanoclusters (CuDTCs), by stabilizing the most thermodynamically and kinetically favored cluster size. Described herein is the synthesis of hydrophilic and hydrophobic CuDTCs and their characterization by electrochemical methods, UV-visible absorption spectroscopy, IR, and ^{1}H-NMR spectroscopy.

4.2 Hydrophobic CuDTCs Stabilized by Durenedithiolate

The ligand chosen for this synthesis is durene-DT, as shown in Figure 24. The linker length between the two thiolates is a four carbon chain, with the two middle carbons belonging to a benzene ring. This semi-rigid structure is proposed to provide excellent stability to the monolayer structure and therefore the Cu cluster as a whole. Also expected is a similarity in

energetics between these CuDTCs and the AuMTCs discussed earlier, particularly the electrochemical behavior resulted from the attached durene-DT ligand.

4.2.1 Synthesis

The synthesis of CuDTCs using durene-DT ligand is described in Figure 24 shown below. The synthetic procedure has evolved substantially from first attempts at this system which included the standard Brust procedure[29] commonly used to synthesize gold nanoclusters and possible one-phase methods, both of which resulted in very low yields and oxidized side products.

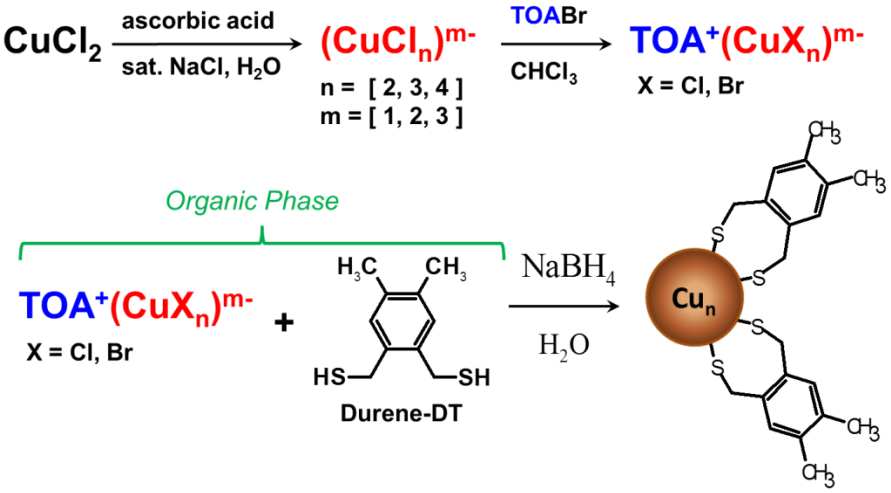

Figure 24. Two-phase synthesis of CuDTCs with durene-DT ligands. Cartoon of cluster is not drawn to scale or indicative of composition.

An important technical detail is the phase-transfer of copper to the organic phase from the aqueous cationic salt ($CuCl_2$). Phase transfer to chloroform organic solvent was achieved by first chemically reducing the copper(II) chloride to colorless copper(I) chloride by the addition of 2 molar equivalents of ascorbic acid in a saturated solution of sodium chloride. The excess chloride anion from saturated NaCl generates the formation of anionic copper(I) chloride complexes ($CuCl_2^-$, $CuCl_3^{2-}$, and $CuCl_4^{3-}$),[125] which are transferred to the chloroform phase by

electrostatic interaction with the TOA cation from TOABr. Copper(II) chloride without reduction by ascorbic acid cannot transfer to the organic phase under similar saturated NaCl conditions, as shown by the overlap of the absorption spectra in the visible range (Figure 25-A). However, if the Cu^{2+} salt is first reduced to Cu^{1+} before phase mixing, then the efficiency of phase transfer is >95% on average, as shown by the difference between copper(II) absorption before and after phase transfer (Figure 25-B).

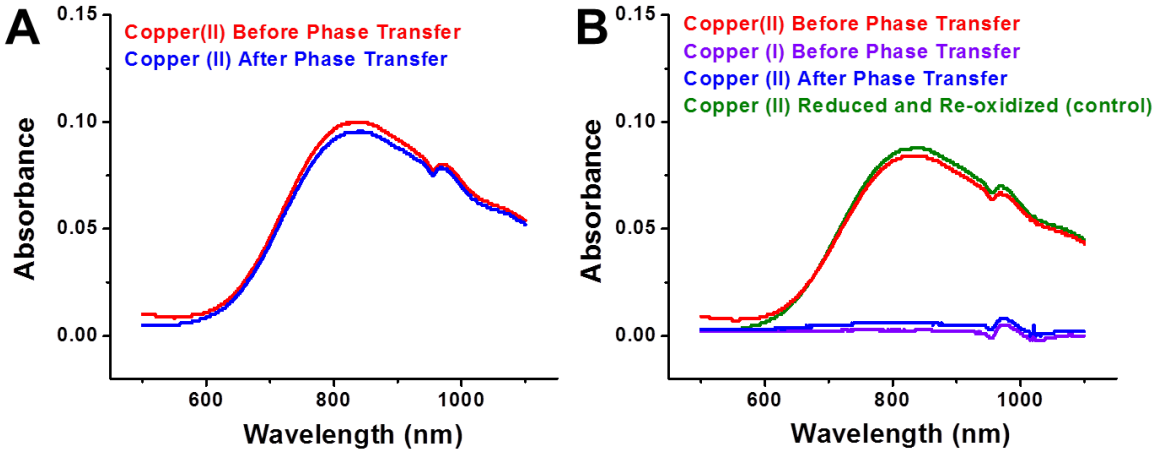

.

Figure 25. (a) Absorption spectra of the aqueous phase during phase transfer of copper cation to the organic phase ($CHCl_3$); copper(II) chloride before phase transfer (red) and copper(II) chloride after phase transfer (blue). **(b)** Absorption spectra of the aqueous phase during phase transfer of copper cation to organic phase ($CHCl_3$) using ascorbic acid reduction procedure; copper(II) chloride before phase transfer (red), copper(I) chloride formed by ascorbic acid reduction before phase transfer (purple), copper(II) chloride formed by H_2O_2 oxidation of copper(I) chloride after phase transfer (blue), and an equimolar solution of copper(II) chloride reduced by ascorbic acid, then oxidized back to copper(II) chloride by H_2O_2 without organic phase mixing (green).

Copper(I) cannot be detected by UV/Vis spectroscopy, as it is colorless and does not absorb in the limits of detection (purple line). Therefore to confirm that no copper is left in the aqueous phase after the procedure, copper(II) is regenerated after reduction to copper(I) by oxidation with 4 molar equivalents of H_2O_2. If an equimolar solution undergoes similar reduction-oxidation procedure without phase mixing (green line), then the result is overlap of the absorption

spectrum with the original copper(II) chloride solution (red line). But if the aqueous phase is re-oxidized after phase transfer, the aqueous phase remains colorless and barely any absorbance is detected (blue line), which confirms that nearly all of the copper(I) has transferred to the organic phase.

After phase transfer, the durene-DT ligand is added to the $TOACuX_n$ salt (X = halide) in chloroform solution, from which no reaction is detected. The formation of CuDTCs is initiated by reduction with sodium borohydride in water. The mechanism of reduction most likely involves the phase transfer of borohydride by TOA cation to the organic phase. During first attempts, toluene was used as the organic solvent. Strangely, toluene was discovered to actually interact and form adducts with the product, so chloroform was selected as the ideal solvent. A more detailed synthetic procedure for the synthesis of durene-DT capped CuDTCs is provided in the experimental section (Appendix E).

4.2.2 Results and Discussion

The proton NMR spectrum for the purified CuDTCs is shown in Figure 26. Each durene-DT proton signal is significantly broadened. The degree of broadening is related to the proximity of the proton to the copper core,[37,108] with the most broadened signal attributed to the methylene protons adjacent to the thiolate group attached to the core. No sharp proton signal or thiol proton signal is detected, which also indicates that each ligand is attached. Infrared spectroscopy further supports that both thiolate groups are attached, as no S-H stretching is observed at ca. 2500 cm^{-1} (Figure 27). TOA^+ proton signal is still present after purification. Note that TOA^+ commonly remains after purification in most Au nanoparticle syntheses and can function as a charge stabilizer for anionic nanoclusters.[40]

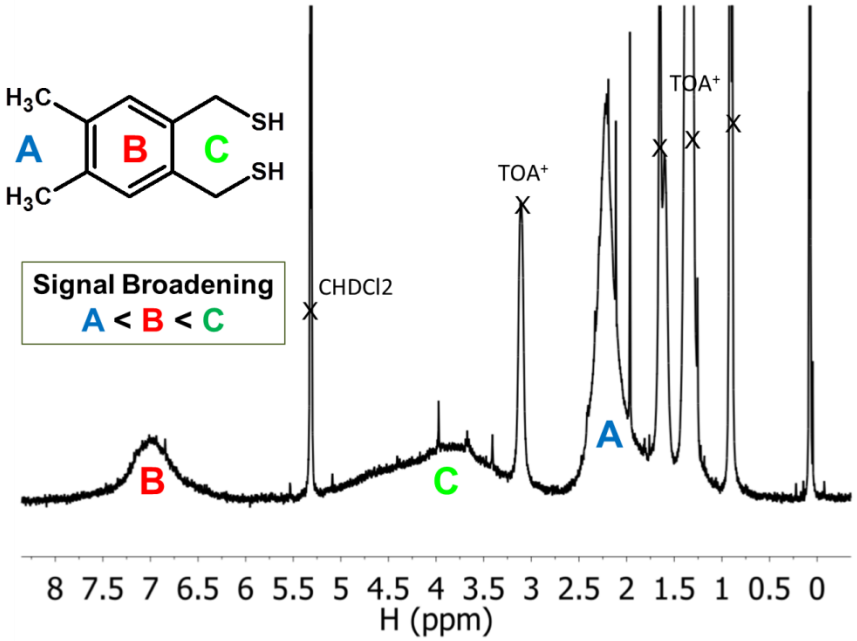

Figure 26. [1]H-NMR spectrum for CuDTCs in deuterated dichloromethane solvent. Structure of durene-DT ligand shown in top left corner.

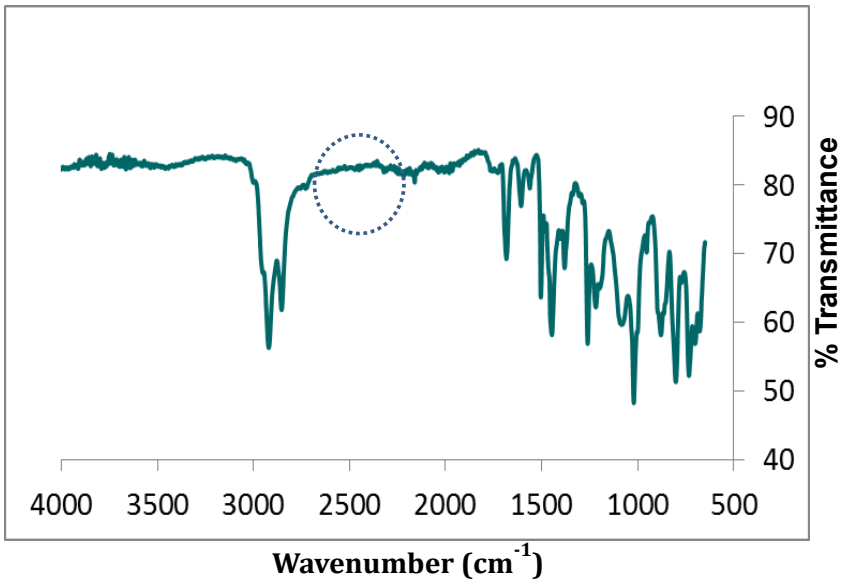

Figure 27. Fourier transform infrared (FTIR) spectrum of CuDTCs. Dashed circle indicates where S-H stretching would be observed for thiol.

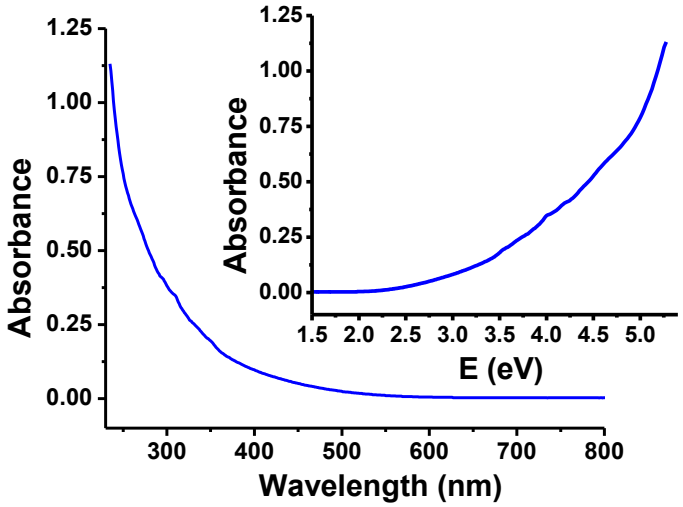

Figure 28. UV/Vis absorption spectrum for purified CuDTCs in dichloromethane.

The UV/Vis absorption spectrum for the CuDTCs is featureless with absorption beginning at ca. 2.1 eV and increasing toward higher energy (Figure 28). The localized surface plasmon resonance for copper nanoparticles results in a well-defined absorption band at ca. 560 nm for particles greater than 20 nm in diameter.[17] This feature is absent from the spectrum of the CuDTCs, which indicates that the clusters are relatively small. Voltammetry of the CuDTCs (Figure 29) reveals two redox potentials in the window of 2 to -2 V, the peak at -1.4 V generating a current about 4-5 times larger than the peak at 0.7 V. The dominant peak is attributed to the reduction of the durene-DT ligand, as discussed in Chapter 2. The HOMO-LUMO band gap is estimated by measuring the spacing between the two peaks of the DPV, giving a value of about 2.1 V, which correlates well to the band edge of the absorption spectrum in Figure 28.

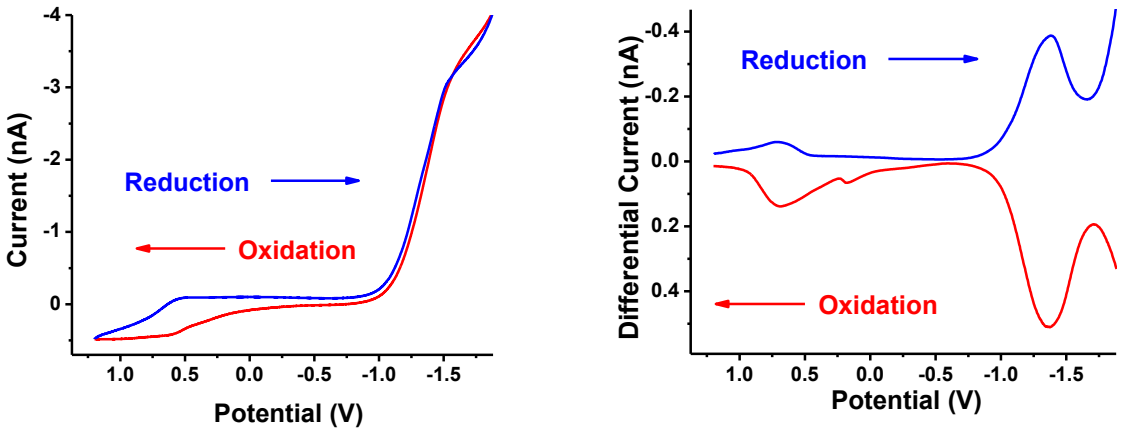

Figure 29. (left) Cyclic voltammogram of CuDTCs in dichloromethane, 100 mV/s scan rate and (right) corresponding differential pulse voltammogram (bottom panel).

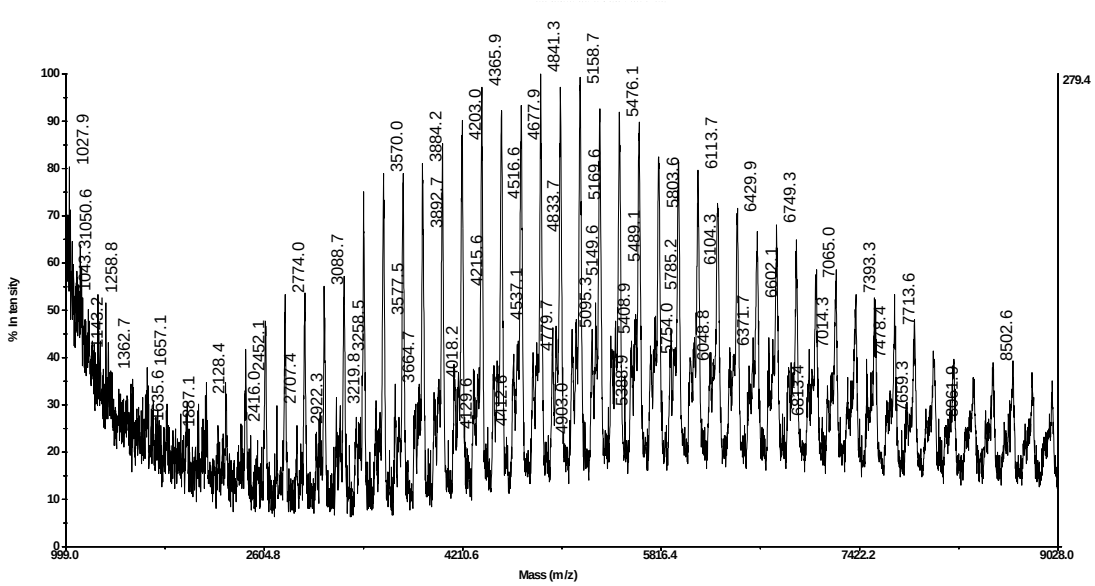

Figure 30. MALDI-MS (+) reflectron mode for CuDTCs with DCTB matrix, laser intensity 5000.

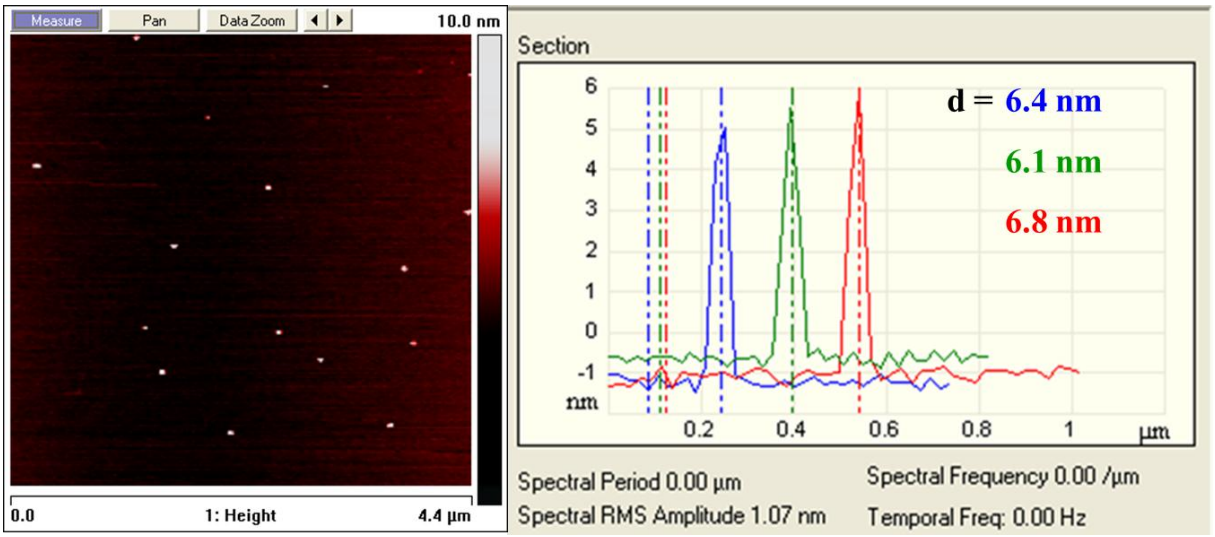

Figure 31. AFM image for CuDTCs and height profiles for three particles.

The MALDI-MS spectrum shown in Figure 30 presents a fragmentation pattern with regular peak spacing of 158-160 m/z, possibly attributed to the neutral mass loss of copper(I) sulfide (Cu_2S) from the monolayer surface. It has been shown for CuMPCs and self-assembled monolayers of thiolate ligands on copper surfaces that upon thermal decomposition, the C-S bond of the ligand actually breaks before the Cu-S bond.[24,109,126] This is due to the strongly covalent character of the Cu-S bond. The Cu_2S fragmentation pattern continues past the m/z limit for reflectron mode, indicating that the molecular ion peak is larger than 10,000 m/z. The AFM image in Figure 31 suggests a relatively monodispersed sample of relatively large particles measuring about 6-7 nm in diameter.

4.2.3 Conclusions

Stable copper nanoclusters averaging six nanometers in diameter were successfully synthesized by a two-phase procedure using durene-DT as the stabilizing ligand. Optical and electrochemical features can be described as molecule-like with an optical band gap of about 2 eV. Lower temperature electrochemical measurements with supporting electrolyte will be

conducted to enhance resolution and establish a more detailed optical-electrochemical correlation. Future work will also include linear mode MALDI-MS with varying laser intensity and screening for possible catalytic activity.

4.3 Hydrophilic CuDTCs Stabilized by Dimercaptosuccinic Acid

The ligand chosen for this synthesis is DMSA, which was mentioned in Chapter 3 to be suitable for the stabilization of monodispersed AgDTCs. The structure, as shown in Figure 32, is a 1,2-substituted dithiol. Since the linker length is only a two-carbon chain, it is very unlikely that any crosslinking can occur between nanoclusters. Crosslinking between clusters is to be avoided since it complicates the synthesis and usually results in large aggregates with poor solubility. This effect has been observed by our group upon attempting AuDTC syntheses using 1,6-hexanedithiol and 1,8-octanedithiol, ligands with relatively long linker chains.

4.3.1 Synthesis

Synthesis of DMSA-protected CuDTCs is outlined in Figure 32. The hydrophilic ligand allows for a simple one-phase synthesis in aqueous solution. However, the order of adding reagents is critical. If DMSA is mixed with the copper(II) chloride salt in water, immediate precipitation occurs due to the formation of large polymeric DMSA-Cu^{+} complexes. The sodium borohydride reducing agent was therefore mixed with the ligand first before the addition of the copper salt. The reaction was rapid, resulting in a dark brown solution, which was purified by dialysis.

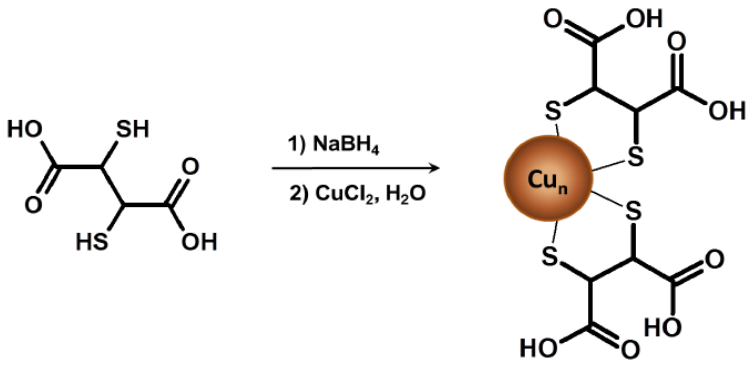

Figure 32. One-phase synthesis of CuDTCs with DMSA ligands. Cartoon of cluster is not drawn to scale or indicative of composition.

4.3.2 Results and Discussion

Only the C-H proton of the DMSA ligand can be detected by ^{1}H-NMR, since the acidic and thiol protons exchange with D_2O (Figure 33). Instead of one broad signal appearing as in the case of durene-DT CuDTCs, the ^{1}H-NMR spectrum for DMSA CuDTCs shows multiple sharp proton signals. No S-H stretching appears in the infrared spectrum, indicating that all thiolate groups are attached (Figure 34). The relative monodispersity of the sample is represented by the AFM image and size histogram in Figure 35.

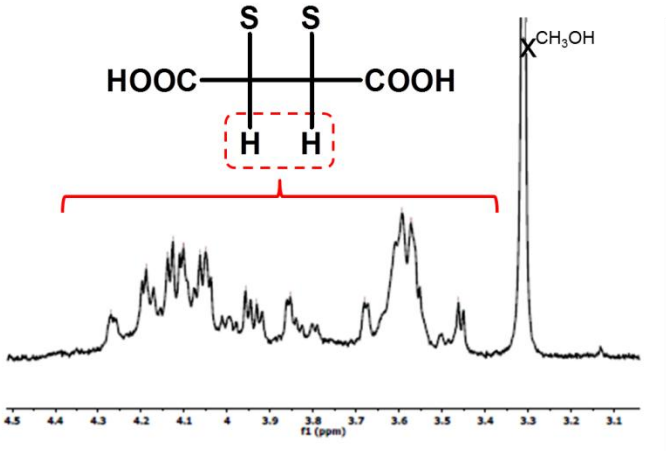

Figure 33. ^{1}H-NMR spectrum for CuDTCs in D_2O. *(Baseline corrected for HOD peak).*

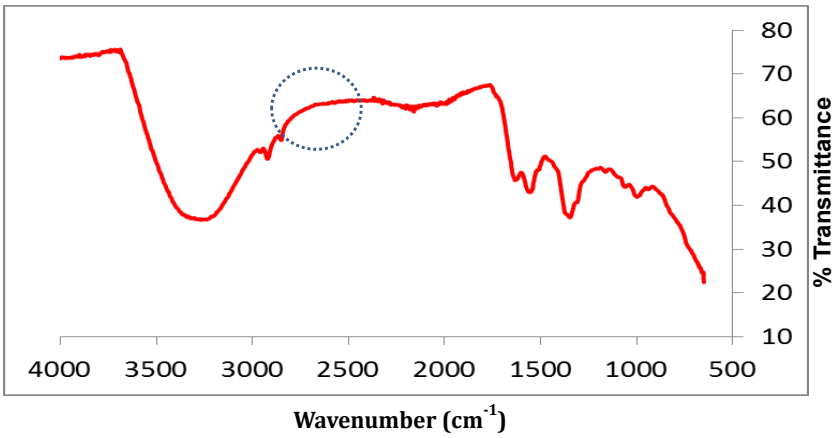

Figure 34. FTIR spectrum for CuDTCs. Dashed circle indicates where S-H stretching would be observed for thiol.

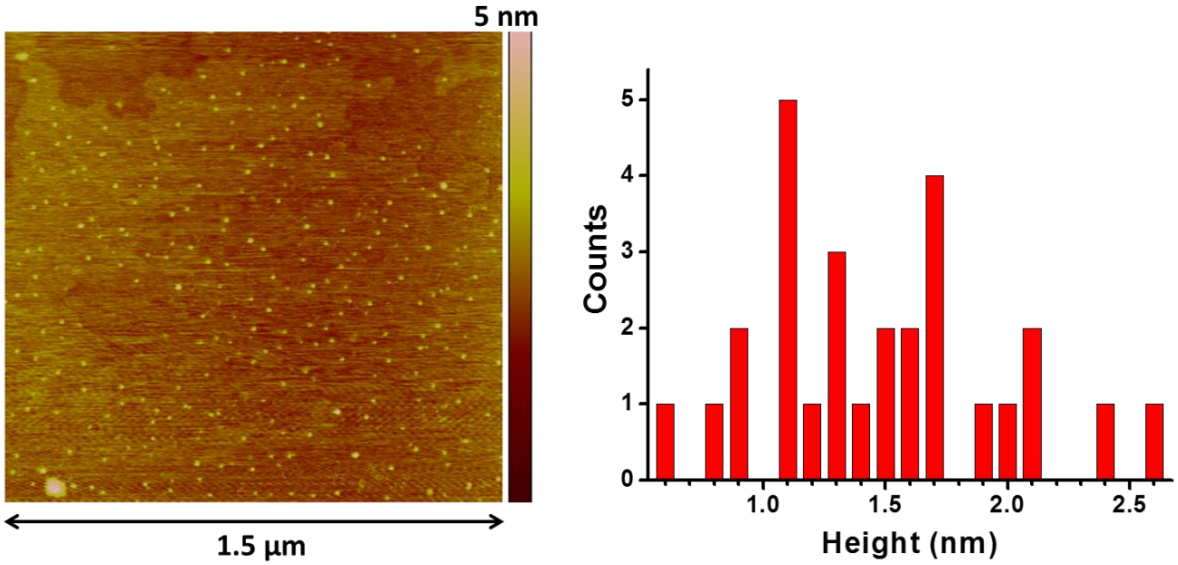

Figure 35. Representative AFM image of CuDTCs (left panel) and histogram showing height distribution for randomly measured particles (right panel).

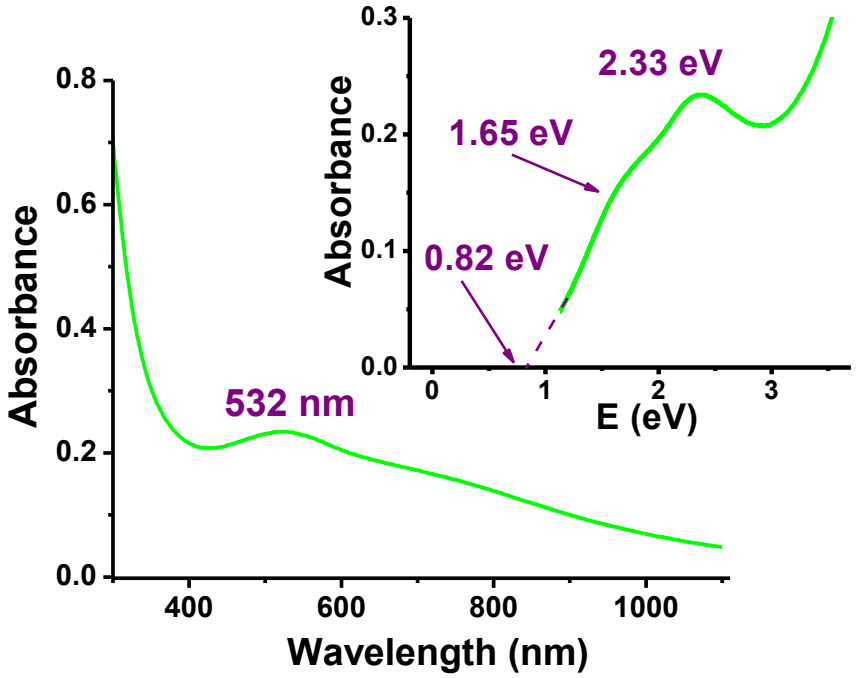

Figure 36. UV/Vis absorption spectrum for purified CuDTCs in water.

As shown in Figure 36, discrete bands are visible in the CuDTC absorption spectrum at 532 nm (2.33 eV) and 753 nm (1.65 eV). A line was extrapolated to estimate a band edge at 0.82 eV, corresponding to the HOMO-LUMO optical band gap. From the oxidation scan of the DPV shown in Figure 37, four different peaks can be resolved, each for a single electron transfer. At negative potential, two peaks are observed corresponding to the two electron quantized charging of an energy level with a measured charging energy (E_{chg}) of 0.19 V. Likewise, two peaks are observed at positive potential with E_{chg} = 0.19 V. The electrochemically measured gap (E_{gap} = 1.01 V) between the negative and positive half-wave potentials closest to the Fermi level is equivalent to the HOMO-LUMO optical band gap value of 0.82 V (E_{opt}) plus the required additional charging energy ($E_{gap} = E_{opt} + E_{chg}$).

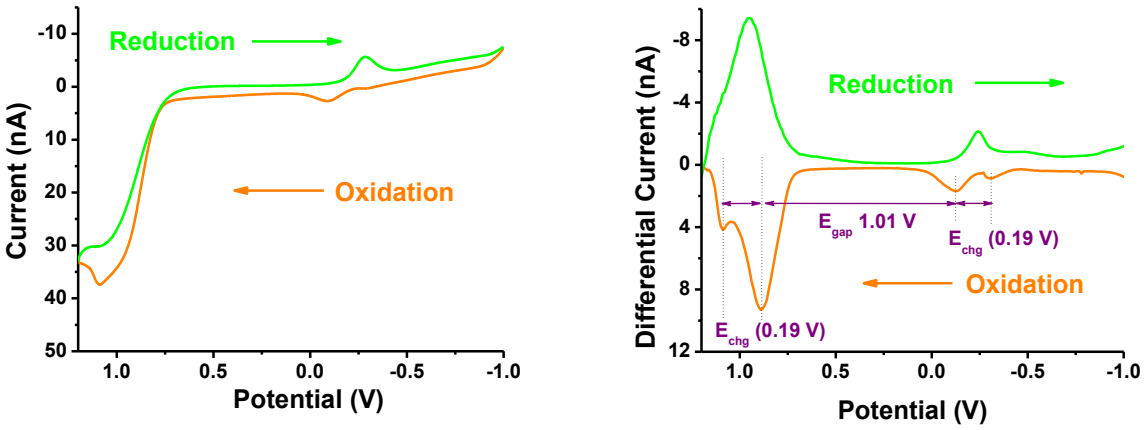

Figure 37. Cyclic voltammogram of CuDTCs in water, 100 mV/s scan rate and corresponding DPV with measured peak spacing.

4.3.3 Conclusions

A one-phase synthesis using DMSA ligand yields monodispersed CuDTCs with discrete energy states. The HOMO-LUMO band gap of 0.82 V was identified by UV/Vis absorption spectroscopy and further supported by voltammetry. Diffusion-ordered spectroscopy (DOSY) will be used to solve for diffusion coefficients useful in electron-transfer quantification and also provide further evidence for the particle size. MALDI-MS and ESI-MS analyses are currently underway.

5. SUMMARY

A new generation of stable metal nanoclusters has been developed by employing dithiolates as the capping ligands. The resulting products of each synthesis all display quantized energy states regardless of metal center or cluster size. Such interesting energetics is proposed to be a result of the interfacial bond structure on the monolayer surface. For nanoclusters synthesized by durene-DT ligation, the energetics was discovered to be substantially affected by the property of the ligand, which was concluded to act as a conducting medium for electron transfer by delocalization in an anionic disulfide radical. Lipoic acid was found to be a favorable ligand for generating relatively small, monodispersed clusters with intense visible luminescence. Dimercaptosuccinic acid was used to stabilize small, monodispersed copper nanoclusters with discrete energetic properties. Larger luminescent copper nanoclusters with interesting electrochemical behavior were formed using durenedithiolate ligand. Efforts are currently focused on determining mass composition by ESI- and MALD-MS, as well as successful crystallization of the nanoclusters to fully resolve their structures and understand the influence of the dithiolate ligands on the properties of metal nanoclusters.

6. REFERENCES

(1) Feldheim, D. L.; Foss, C. A. *Metal Nanoparticles: Synthesis, Characterization, and Applications*; Marcel Dekker, 2002.

(2) Daniel, M.-C.; Astruc, D. *Chem. Rev.* **2003**, *104*, 293.

(3) Dhar, S.; Daniel, W. L.; Giljohann, D. A.; Mirkin, C. A.; Lippard, S. J. *J. Am. Chem. Soc.* **2009**, *131*, 14652.

(4) Jones, M. R.; Osberg, K. D.; Macfarlane, R. J.; Langille, M. R.; Mirkin, C. A. *Chem. Rev.* **2011**, *111*, 3736.

(5) Burda, C.; Chen, X.; Narayanan, R.; El-Sayed, M. A. *Chem. Rev.* **2005**, *105*, 1025.

(6) Murray, R. W. *Chem. Rev.* **2008**, *108*, 2688.

(7) Heiz, U.; Landman, U. *Nanocatalysis*; Springer-Verlag, 2007.

(8) Donkers, R. L.; Lee, D.; Murray, R. W. *Langmuir* **2004**, *20*, 1945.

(9) Wu, Z.; Suhan, J.; Jin, R. *J. Mater. Chem.* **2009**, *19*, 622.

(10) Zhu, M.; Lanni, E.; Garg, N.; Bier, M. E.; Jin, R. *J. Am. Chem. Soc.* **2008**, *130*, 1138.

(11) Whetten, R. L.; Price, R. C. *Science (Washington, DC, U. S.)* **2007**, *318*, 407.

(12) Jin, R.; Qian, H.; Wu, Z.; Zhu, Y.; Zhu, M.; Mohanty, A.; Garg, N. *J. Phys. Chem. Lett.* **2010**, *1*, 2903.

(13) Wang, W.; Chen, X.; Efrima, S. *J. Phys. Chem. B* **1999**, *103*, 7238.

(14) Jana, N. R.; Gearheart, L.; Murphy, C. J. *J. Phys. Chem. B* **2001**, *105*, 4065.

(15) Leff, D. V.; Brandt, L.; Heath, J. R. *Langmuir* **1996**, *12*, 4723.

(16) Kumar, A.; Mandal, S.; Pasricha, R.; Mandale, A. B.; Sastry, M. *Langmuir* **2003**, *19*, 6277.

(17) Wang, Y.; Asefa, T. *Langmuir* **2010**, *26*, 7469.

(18) Garcia-Martinez, J. C.; Crooks, R. M. *J. Am. Chem. Soc.* **2004**, *126*, 16170.

(19) Wilson, O. M.; Scott, R. W. J.; Garcia-Martinez, J. C.; Crooks, R. M. *J. Am. Chem. Soc.* **2004**, *127*, 1015.

(20) Scott, R. W. J.; Wilson, O. M.; Oh, S.-K.; Kenik, E. A.; Crooks, R. M. *J. Am. Chem. Soc.* **2004**, *126*, 15583.

(21) Schwarzenbach, G. *Helv. Chim. Acta* **1952**, *35*, 2344.

(22) Love, J. C.; Estroff, L. A.; Kriebel, J. K.; Nuzzo, R. G.; Whitesides, G. M. *Chem. Rev. (Washington, DC, U. S.)* **2005**, *105*, 1103.

(23) Nuzzo, R. G.; Allara, D. L. *J. Am. Chem. Soc.* **1983**, *105*, 4481.

(24) Konôpka, M.; Rousseau, R.; Štich, I.; Marx, D. *J. Am. Chem. Soc.* **2004**, *126*, 12103.

(25) Kumar, A.; Mandale, A. B.; Sastry, M. *Langmuir* **2000**, *16*, 6921.

(26) Crooks, R. M.; Zhao, M.; Sun, L.; Chechik, V.; Yeung, L. K. *Acc. Chem. Res.* **2000**, *34*, 181.

(27) Brust, M.; Walker, M.; Bethell, D.; Schiffrin, D. J.; Whyman, R. *J. Chem. Soc.-Chem. Comm.* **1994**, 801.

(28) Rowe, M. P.; Plass, K. E.; Kim, K.; Kurdak, Ç.; Zellers, E. T.; Matzger, A. J. *Chem. Mater.* **2004**, *16*, 3513.

(29) Brust, M.; Fink, J.; Bethell, D.; Schiffrin, D. J.; Kiely, C. *J. Chem. Soc.- Chem. Comm.* **1995**, 1655.

(30) Templeton, A. C.; Chen, S.; Gross, S. M.; Murray, R. W. *Langmuir* **1999**, *15*, 66.

(31) Cliffel, D. E.; Zamborini, F. P.; Gross, S. M.; Murray, R. W. *Langmuir* **2000**, *16*, 9699.

(32) Tang, Z. X., B.; Wu, B.; Germann, M. W.; Wang, G. *J. Am. Chem. Soc.* **2010**, *132*, 3367.

(33) Goulet, P. J. G.; Lennox, R. B. *J. Am. Chem. Soc.* **2010**, *132*, 9582.
(34) Li, Y.; Zaluzhna, O.; Xu, B.; Gao, Y.; Modest, J. M.; Tong, Y. Y. J. *J. Am. Chem. Soc.* **2011**, *133*, 2092.
(35) Li, Y.; Zaluzhna, O.; Tong, Y. Y. J. *Langmuir* **2011**, *27*, 7366.
(36) Parker, J. F.; Weaver, J. E. F.; McCallum, F.; Fields-Zinna, C. A.; Murray, R. W. *Langmuir* **2010**, *26*, 13650.
(37) Hostetler, M. J.; Wingate, J. E.; Zhong, C. J.; Harris, J. E.; Vachet, R. W.; Clark, M. R.; Londono, J. D.; Green, S. J.; Stokes, J. J.; Wignall, G. D.; Glish, G. L.; Porter, M. D.; Evans, N. D.; Murray, R. W. *Langmuir* **1998**, *14*, 17.
(38) Hussain, I.; Graham, S.; Wang, Z.; Tan, B.; Sherrington, D. C.; Rannard, S. P.; Cooper, A. I.; Brust, M. *J. Am. Chem. Soc.* **2005**, *127*, 16398.
(39) Jiang, D.-e.; Tiago, M. L.; Luo, W.; Dai, S. *J. Am. Chem. Soc.* **2008**, *130*, 2777.
(40) Heaven, M. W.; Dass, A.; White, P. S.; Holt, K. M.; Murray, R. W. *J. Am. Chem. Soc.* **2008**, *130*, 3754.
(41) Zhu, M.; Aikens, C. M.; Hollander, F. J.; Schatz, G. C.; Jin, R. *J. Am. Chem. Soc.* **2008**, *130*, 5883.
(42) Qian, H. F.; Eckenhoff, W. T.; Zhu, Y.; Pintauer, T.; Jin, R. C. *J. Am. Chem. Soc.* **2010**, *132*, 8280.
(43) Jadzinsky, P. D.; Calero, G.; Ackerson, C. J.; Bushnell, D. A.; Kornberg, R. D. *Science* **2007**, *318*, 430.
(44) Negishi, Y.; Takasugi, Y.; Sato, S.; Yao, H.; Kimura, K.; Tsukuda, T. *J. Am. Chem. Soc.* **2004**, *126*, 6518.
(45) Parker, J. F.; Fields-Zinna, C. A.; Murray, R. W. *Acc. Chem. Res.* **2010**, *43*, 1289.
(46) Parker, J. F.; Weaver, J. E. F.; McCallum, F.; Fields-Zinna, C. A.; Murray, R. W. *Langmuir* **2010**, *26*, 13650.
(47) Daniel, M.-C.; Astruc, D. *Chem. Rev.* **2004**, *104*, 293.
(48) Sardar, R.; Funston, A. M.; Mulvaney, P.; Murray, R. W. *Langmuir* **2009**, *25*, 13840.
(49) Qian, H. J., R. *Nano. Lett.* **2009**, *9*, 4083.
(50) Donkers, R. L.; Lee, D.; Murray, R. W. *Langmuir* **2004**, *20*, 1945.
(51) Hicks, J. F.; Miles, D. T.; Murray, R. W. *J. Am. Chem. Soc.* **2002**, *124*, 13322.
(52) Lee, D.; Donkers, R. L.; Wang, G. L.; Harper, A. S.; Murray, R. W. *J. Am. Chem. Soc.* **2004**, *126*, 6193.
(53) Wang, G.; Huang, T.; Murray, R. W.; Menard, L.; Nuzzo, R. G. *J. Am. Chem. Soc.* **2005**, *127*, 812.
(54) Wang, G. L.; Guo, R.; Kalyuzhny, G.; Choi, J. P.; Murray, R. W. *J. Phys. Chem. B* **2006**, *110*, 20282.
(55) Montalti, M.; Zaccheroni, N.; Prodi, L.; O'Reilly, N.; James, S. L. *J. Am. Chem. Soc.* **2007**, *129*, 2418.
(56) Tang, Z. X., B.; Wu, B.; Robinson, D. A.; Bokossa, N.; Wang, G. *Langmuir* **2011**, *27*, 2989.
(57) Wu, Z. J., R. *Nano. Lett.* **2010**, *10*, 2568.
(58) Devadas, M. S.; Kim, J.; Sinn, E.; Lee, D.; Goodson, T.; Ramakrishna, G. *J. Phys. Chem. C* **2010**, *114*, 22417.
(59) Canzi, G.; Mrse, A. A.; Kubiak, C. P. *J. Phys. Chem. C* **2011**, *115*, 7972.
(60) Hu, J.; Zhang, Y.; Liu, B.; Liu, J.; Zhou, H.; Xu, Y.; Jiang, Y.; Yang, Z.; Tian, Z.-Q. *J. Am. Chem. Soc.* **2004**, *126*, 9470.

(61) Dass, A.; Stevenson, A.; Dubay, G. R.; Tracy, J. B.; Murray, R. W. *J. Am. Chem. Soc.* **2008**, *130*, 5940.

(62) Chaki, N. K.; Negishi, Y.; Tsunoyama, H.; Shichibu, Y.; Tsukuda, T. *J. Am. Chem. Soc.* **2008**, *130*, 8608.

(63) Dharmaratne, A. C. K., T.; Dass, A. *J. Am. Chem. Soc.* **2009**, *131*, 13604.

(64) Fang, S.; Lee, H. J.; Wark, A. W.; Corn, R. M. *J. Am. Chem. Soc.* **2006**, *128*, 14044.

(65) Gifford, L. K.; Sendroiu, I. E.; Corn, R. M.; Lupták, A. *J. Am. Chem. Soc.* **2010**, *132*, 9265.

(66) Sendroiu, I. E.; Gifford, L. K.; Lupták, A.; Corn, R. M. *J. Am. Chem. Soc.* **2011**, *133*, 4271.

(67) Kamat, P. V. *J. Phys. Chem. C* **2007**, *111*, 2834.

(68) Pradhan, S.; Ghosh, D.; Chen, S. *ACS App. Mater. & Inter.* **2009**, *1*, 2060.

(69) Valden, M.; Lai, X.; Goodman, D. W. *Science* **1998**, *281*, 1647.

(70) Yagi, I.; Ishida, T.; Uosaki, K. *Electrochem. Comm.* **2004**, *6*, 773.

(71) Tang, W.; Lin, H.; Kleiman-Shwarsctein, A.; Stucky, G. D.; McFarland, E. W. *J. Phys. Chem. C* **2008**, *112*, 10515.

(72) Chen, W.; Chen, S. *Angew. Chem., Int. Ed.* **2009**, *48*, 4386.

(73) Li, Y.; Cox, J. T.; Zhang, B. *J. Am. Chem. Soc.* **2010**, *132*, 3047.

(74) Zhu, Y.; Qian, H.; Drake, B. A.; Jin, R. *Angew. Chem., Int. Ed.* **2010**, *49*, 1295.

(75) Hayakawa, K.; Yoshimura, T.; Esumi, K. *Langmuir* **2003**, *19*, 5517.

(76) Mohr, C.; Hofmeister, H.; Radnik, J.; Claus, P. *J. Am. Chem. Soc.***2003**, *125*, 1905.

(77) Claus, P.; Brückner, A.; Mohr, C.; Hofmeister, H. *J. Am. Chem. Soc.* **2000**, *122*, 11430.

(78) Andreeva, D.; Tabakova, T.; Idakiev, V.; Christov, P.; Giovanoli, R. *App. Cat. A: Gen.* **1998**, *169*, 9.

(79) Valden, M. L., X. *Science* **1998**, *281*, 1647.

(80) Kozlova, A. P.; Kozlov, A. I.; Sugiyama, S.; Matsui, Y.; Asakura, K.; Iwasawa, Y. *J. Cat.* **1999**, *181*, 37.

(81) Guczi, L.; Horváth, D.; Pászti, Z.; Tóth, L.; Horváth, Z. E.; Karacs, A.; Petõ, G. *J. Phys. Chem. B* **2000**, *104*, 3183.

(82) M. Finch, R.; A. Hodge, N.; J. Hutchings, G.; Meagher, A.; A. Pankhurst, Q.; Rafiq H. Siddiqui, M.; E. Wagner, F.; Whyman, R. *Phys. Chem. Chem. Phys.* **1999**, *1*, 485.

(83) Herzing, A. A.; Kiely, C. J.; Carley, A. F.; Landon, P.; Hutchings, G. J. *Science* **2008**, *321*, 1331.

(84) Hayden, B. E.; Pletcher, D.; Suchsland, J.-P. *Angew. Chem.* **2007**, *119*, 3600.

(85) Henglein, A. *Chem. Mater.* **1998**, *10*, 444.

(86) Zhang, J.; Fu, Y.; Chowdhury, M. H.; Lakowicz, J. R. *J. Phys. Chem. C* **2007**, *112*, 18.

(87) Maretti, L.; Billone, P. S.; Liu, Y.; Scaiano, J. C. *J. Am. Chem. Soc.* **2009**, *131*, 13972.

(88) Esumi, K.; Suzuki, A.; Yamahira, A.; Torigoe, K. *Langmuir* **2000**, *16*, 2604.

(89) Zheng, J.; Dickson, R. M. *J. Am. Chem. Soc.* **2002**, *124*, 13982.

(90) Rao, T. U. B.; Nataraju, B.; Pradeep, T. *J. Am. Chem. Soc.* **2010**, *132*, 16304.

(91) Cathcart, N.; Mistry, P.; Makra, C.; Pietrobon, B.; Coombs, N.; Jelokhani-Niaraki, M.; Kitaev, V. *Langmuir* **2009**, *25*, 5840.

(92) Cathcart, N.; Kitaev, V. *J. Phys. Chem. C* **2010**, *114*, 16010.

(93) Kang, S. Y.; Kim, K. *Langmuir* **1998**, *14*, 226.

(94) Shon, Y. S.; Gross, S. M.; Dawson, B.; Porter, M.; Murray, R. W. *Langmuir* **2000**, *16*, 6555.

(95) Zheng, J.; Ding, Y.; Tian, B.; Wang, Z. L.; Zhuang, X. *J. Am. Chem. Soc.* **2008**, *130*, 10472.

(96) Bakr, O. M.; Amendola, V.; Aikens, C. M.; Wenseleers, W.; Li, R.; Dal Negro, L.; Schatz, G. C.; Stellacci, F. *Angew. Chem. Int. Ed.* **2009**, *48*, 5921.

(97) Kumar, S.; Bolan, M. D.; Bigioni, T. P. *J. Am. Chem. Soc.* **2010**, *132*, 13141.

(98) Wu, Z. L., E.; Chen, W.; Bier, M. E.;Ly, D.; Jin, R. *J. Am. Chem. Soc.* **2009**, *131*, 16672.

(99) Vilar-Vidal, N.; Blanco, M. C.; López-Quintela, M. A.; Rivas, J.; Serra, C. *J. Phys. Chem. C* **2010**, *114*, 15924.

(100) Huang, H. H.; Yan, F. Q.; Kek, Y. M.; Chew, C. H.; Xu, G. Q.; Ji, W.; Oh, P. S.; Tang, S. H. *Langmuir* **1997**, *13*, 172.

(101) Liu, Z.; Yang, Y.; Liang, J.; Hu, Z.; Li, S.; Peng, S.; Qian, Y. *J. Phys. Chem. B* **2003**, *107*, 12658.

(102) Wu, S.-H.; Chen, D.-H. *J. Colloid Interface Sci.* **2004**, *273*, 165.

(103) Chang, Y.; Lye, M. L.; Zeng, H. C. *Langmuir* **2005**, *21*, 3746.

(104) Zhou, G.; Lu, M.; Yang, Z. *Langmuir* **2006**, *22*, 5900.

(105) Bozzini, B.; D'Urzo, L.; Re, M.; Riccardis, F. *J. Appl. Electrochem.* **2008**, *38*, 1561.

(106) Ziegler, K. J.; Doty, R. C.; Johnston, K. P.; Korgel, B. A. *J. Am. Chem. Soc.* **2001**, *123*, 7797.

(107) Chen, S.; Sommers, J. M. *J. Phys. Chem. B* **2001**, *105*, 8816.

(108) Dong, T.-Y.; Wu, H.-H.; Lin, M.-C. *Langmuir* **2006**, *22*, 6754.

(109) Mott, D.; Yin, J.; Engelhard, M.; Loukrakpam, R.; Chang, P.; Miller, G.; Bae, I.-T.; Chandra Das, N.; Wang, C.; Luo, J.; Zhong, C.-J. *Chem. Mater.* **2009**, *22*, 261.

(110) Wei, W.; Lu, Y.; Chen, W.; Chen, S. *J. Am. Chem. Soc.* **2011**, *133*, 2060.

(111) Alonso, F.; Moglie, Y.; Radivoy, G.; Yus, M. *Tetra. Lett.* **2009**, *50*, 2358.

(112) Sharghi, H.; Khalifeh, R.; Doroodmand, M. M. *Adv. Synth. Catal.* **2009**, *351*, 207.

(113) Singh, P.; Kumari, K.; Katyal, A.; Kalra, R.; Chandra, R. *Catal. Lett.* **2009**, *127*, 119.

(114) Park, J. B.; Graciani, J.; Evans, J.; Stacchiola, D.; Senanayake, S. D.; Barrio, L.; Liu, P.; Sanz, J. F.; Hrbek, J.; Rodriguez, J. A. *J. Am. Chem. Soc.* **2010**, *132*, 356.

(115) Negishi, Y.; Tsukuda, T. *J. Am. Chem. Soc.* **2003**, *125*, 4046.

(116) Abad, J. M.; Mertens, S. F. L.; Pita, M.; Fernández, V. M.; Schiffrin, D. J. *J. Am. Chem. Soc.* **2005**, *127*, 5689.

(117) Zhang, S.; Leem, G.; Srisombat, L.-o.; Lee, T. R. *J. Am. Chem. Soc.* **2008**, *130*, 113.

(118) Wu, Z.; Lanni, E.; Chen, W.; Bier, M. E.; Ly, D.; Jin, R. *J. Am. Chem. Soc.* **2009**, *131*, 16672.

(119) Tang, Z. R., D. A.; Bokossa, N.; Xu, B.; Wang, S.; Wang, G. *J. Am. Chem. Soc.* **2011**, *under review*.

(120) Mortensen, J.; Heinze, J. *Angew. Chem.* **1984**, *96*, 64.

(121) Gilbert, B. C.; Laue, H. A. H.; Norman, R. O. C.; Sealy, R. C. *J. Chem. Soc., Perkin Trans. 2* **1975**, 892.

(122) Mason, R. P.; Chignell, C. F. *Pharm. Rev.* **1981**, *33*, 189.

(123) Bard, A. J. F., L. R. *Electrochemical Methods: Fundamentals and Applications, 2nd Ed.*; Wiley: New York, 2001.

(124) Olynick, D. L.; Gibson, J. M.; Averback, R. S. *Appl. Phys. Lett.* **1996**, *68*, 343.

(125) Liu, W.; Brugger, J.; McPhail, D. C.; Spiccia, L. *Geoch. et Cosm. Acta* **2002**, *66*, 3615.

(126) Konopka, M.; Turansky, R.; Reichert, J.; Fuchs, H.; Marx, D.; Scarontich, I. *Phys. Rev. Lett.* **2008**, *100*, 115503.

7. APPENDICES

A. Chemicals

Copper(II) chloride ($CuCl_2$, 99.9%), silver nitrate ($AgNO_3$, 99.9%), tetrachloroauric acid trihydrate ($HAuCl_4 \cdot 3H_2O$, >99.99% metals basis), sodium chloride (NaCl, 99.9%), ascorbic acid (99%), sodium borohydride (99%), 2-Phenylethanethiol (>99%), dimercaptosuccinic acid (DMSA, 99.8%), alpha-lipoic acid (LA, 99%), tetrabutylammonium perchlorate (TBAP, >99%), tetraoctylammonium bromide (TOABr, 98%), *trans*-2-[3-(4-tert-butylphenyl)-2-methyl-propenylidene]-malononitrile (DCTB, >99%), and organic solvents (HPLC grade) were used as received from Sigma-Aldrich. Durene-α1, α2-dithiol (>95%) was from TCI-America.

B. Measurements

UV-visible absorbance spectra were recorded with a Shimadzu UV-1700 spectrophotometer. Luminescence was measured with a Horiba Jobin-Yvon Fluorolog 311 spectrometer with T channel, through which a visible PMT detector and a near IR InGaAs detector were attached. MALDI mass spectra were acquired with ABI 4800 matrix assisted laser desorption ionization (MALDI) TOF-TOF analyzer, with DCTB as matrix. Proton NMR spectra were acquired on a Bruker Avance 400 MHz spectrometer in CD_2Cl_2. A CH instrument 700C electrochemical workstation was used in electrochemical measurements. The working electrode was a 20 micron Pt disk electrode. Ag/AgCl wire as reference electrode was calibrated in 2 mM ferrocene with 0.1 M TBAP solution prior to use. Each sample solution was degassed under Argon prior to measurement.

C. Synthesis of AuMTCs

The AuMTCs were synthesized via a modified two phase Brust-Schiffrin method. In a typical experiment, gold salt ($HAuCl_4 \cdot 3H_2O$) was first phase-transferred from an aqueous solution to a toluene solution with TOABr. The organic layer was separated, and then a mixed thiol solution (Durene-DT: PhC2S: Au= 1: 2: 1) was added in at moderate magnetic stirring. The solution color changed from gold yellow to colorless in ~30 mins. Then freshly prepared $NaBH_4$ (20 equivalents of gold) aqueous solution was added quickly while vigorously stirring. The solution turned black immediately. After the reaction was completed in 1-3 days monitored by absorbance transition, the organic layer was separated and washed by water 3-5 times. The solvent was removed by rotary evaporator, and the product was first precipitated by methanol, while the methanol solution was filtered away. The black solid was further rinsed with copious acetonitrile (stirring overnight) to remove the extra free ligand molecules. The leftover black solid is collected as final MTCs product.

D. Synthesis of LA AgDTCs

LA (0.2 mmol, 40 mg) was dissolved in 5 mL of 25 mM NaOH solution. A solution of $AgNO_3$ (0.1 mmol, 17 mg) in 5 mL 25 mM NaOH was mixed with the LA solution at moderate stirring for 15 minutes. NaBH4 (40 mg) in 10 mL of 25 mM NaOH is added to the mixture at rapid magnetic stir speed and the reaction is completed within 12 hours, resulting in a vibrant reddish orange colored solution.

E. Synthesis of Durene-DT CuDTCs

$CuCl_2$ (0.1 mmol, 13.5 mg) and ascorbic acid (0.4 mmol, 66 mg) were co-dissolved in a saturated NaCl solution (10 mL), resulting in a colorless solution of copper(I) chloride (CuCl). A

solution of TOABr (0.2 mmol, 109 mg) in 10 mL chloroform was mixed with the CuCl aqueous solution for five minutes under rapid stirring to bring Cu^{+} into the organic phase. A solution of Durene-DT (0.1 mmol, 20 mg) in 10 mL chloroform was added, followed by a solution of sodium borohydride (20 mg) in 10 mL water under vigorous stirring. The reaction conditions were maintained for 12 hours. After reaction completion, the organic phase was washed three times with water and concentrated to an orange solid residue by rotary evaporation. The dried CuDTCs were then dissolved in acetonitrile and allowed to precipitate out within 48 hours, after which they are filtered and washed three times with acetonitrile.

F. Synthesis of DMSA CuDTCs

A 5 mL aqueous solution of DMSA (0.3 mmol, 54 mg) was slowly added to a 5 mL aqueous solution of sodium borohydride (100 mg) under moderate stirring. A solution of $CuCl_2$ (0.1 mmol, 13.5 mg) in 10 mL water was added dropwise to the reaction flask with vigorous magnetic stirring. After 1 hour, the reaction was complete. The dark brown CuDTC solution was adjusted to pH 1 with HCl and dialyzed for three days using 3500 MW snakeskin tubing.